NAVAL POSTGRADUATE SCHOOL

MONTEREY, CALIFORNIA

THESIS

REDUCTION EXPANSION SYNTHESIS OF SINTERED METAL

by

Wilson L. Rydalch

June 2019

Thesis Advisor: Jonathan Phillips
Co-Advisor: Claudia C. Luhrs

THIS PAGE INTENTIONALLY LEFT BLANK

REPORT DOCUMENTATION PAGE			*Form Approved OMB No. 0704-0188*

1. AGENCY USE ONLY *(Leave blank)*	**2. REPORT DATE** June 2019	**3. REPORT TYPE AND DATES COVERED** Master's thesis

4. TITLE AND SUBTITLE REDUCTION EXPANSION SYNTHESIS OF SINTERED METAL	**5. FUNDING NUMBERS**
6. AUTHOR(S) Wilson L. Rydalch	
7. PERFORMING ORGANIZATION NAME(S) AND ADDRESS(ES) Naval Postgraduate School Monterey, CA 93943-5000	**8. PERFORMING ORGANIZATION REPORT NUMBER**
9. SPONSORING / MONITORING AGENCY NAME(S) AND ADDRESS(ES) N/A	**10. SPONSORING / MONITORING AGENCY REPORT NUMBER**

11. SUPPLEMENTARY NOTES The views expressed in this thesis are those of the author and do not reflect the official policy or position of the Department of Defense or the U.S. Government.

12a. DISTRIBUTION / AVAILABILITY STATEMENT Approved for public release. Distribution is unlimited.	**12b. DISTRIBUTION CODE** A

13. ABSTRACT (maximum 200 words)

In this work we demonstrate that the unique Reduction Expansion Synthesis-Sintered Metal (RES-SM) technique can be employed to create sintered nickel and iron bodies at hundreds of degrees below their melting temperature. The first process step is "activating" the metal powder in a bath of hydrogen peroxide. In the second step activated metal powder is mixed with the corresponding metal oxide powder. The mixed powder is used to fill a 3D-printed plastic mold. Next, the oxidized metal powder and the metal oxide powder are reduced through the chemical process that takes place with the exposure of the decomposition of urea. The thermal decomposition of urea produces radical species that reduce the metal particles. Optimal results were achieved by heating the powder shapes to 900 degrees Celsius for 1200 seconds in an inert atmosphere with nitrogen gas flowing. Inspection using scanning electron microscopy revealed that the metals samples were held together by necking in between the metal particles. X-ray powder diffraction confirmed that the RES-SM technique produced a completely reduced metal sample. The samples produced in the study are completely self-supporting, but they are similar to metal parts that require post-processing to fully densify, also known as "green" metal parts. Green metal parts are generally understood to not be as hard, dense, or ductile as metal parts. However, the post-processing procedures for green metal parts are widely understood, and can be applied.

14. SUBJECT TERMS metal additive manufacturing, additive manufacturing, low temperature casting, metal powder sintering, Reduction Expansion Synthesis-Sintered Metals	**15. NUMBER OF PAGES** 85
	16. PRICE CODE

17. SECURITY CLASSIFICATION OF REPORT	**18. SECURITY CLASSIFICATION OF THIS PAGE**	**19. SECURITY CLASSIFICATION OF ABSTRACT**	**20. LIMITATION OF ABSTRACT**
Unclassified	Unclassified	Unclassified	UU

NSN 7540-01-280-5500 Standard Form 298 (Rev. 2-89) Prescribed by ANSI Std. 239-18

THIS PAGE INTENTIONALLY LEFT BLANK

Approved for public release. Distribution is unlimited.

REDUCTION EXPANSION SYNTHESIS OF SINTERED METAL

Wilson L. Rydalch
Lieutenant Junior Grade, United States Navy
BSME, U.S. Naval Academy, 2017

Submitted in partial fulfillment of the
requirements for the degree of

MASTER OF SCIENCE IN MECHANICAL ENGINEERING

from the

NAVAL POSTGRADUATE SCHOOL
June 2019

Approved by: Jonathan Phillips
Advisor

Claudia C. Luhrs
Co-Advisor

Garth V. Hobson
Chair, Department of Mechanical and Aerospace Engineering

THIS PAGE INTENTIONALLY LEFT BLANK

ABSTRACT

In this work we demonstrate that the unique Reduction Expansion Synthesis-Sintered Metal (RES-SM) technique can be employed to create sintered nickel and iron bodies at hundreds of degrees below their melting temperature. The first process step is “activating” the metal powder in a bath of hydrogen peroxide. In the second step activated metal powder is mixed with the corresponding metal oxide powder. The mixed powder is used to fill a 3D-printed plastic mold. Next, the oxidized metal powder and the metal oxide powder are reduced through the chemical process that takes place with the exposure of the decomposition of urea. The thermal decomposition of urea produces radical species that reduce the metal particles. Optimal results were achieved by heating the powder shapes to 900 degrees Celsius for 1200 seconds in an inert atmosphere with nitrogen gas flowing. Inspection using scanning electron microscopy revealed that the metals samples were held together by necking in between the metal particles. X-ray powder diffraction confirmed that the RES-SM technique produced a completely reduced metal sample. The samples produced in the study are completely self-supporting, but they are similar to metal parts that require post-processing to fully densify, also known as “green” metal parts. Green metal parts are generally understood to not be as hard, dense, or ductile as metal parts. However, the post-processing procedures for green metal parts are widely understood, and can be applied.

THIS PAGE INTENTIONALLY LEFT BLANK

TABLE OF CONTENTS

I. INTRODUCTION....1
A. CURRENT M-AM TECHNOLOGIES....2
B. METAL ADDITIVE MANUFACTURING NEEDS IN UNITED STATES NAVY....4
C. REDUCTION EXPANSION SYNTHESIS....6
D. OBJECTIVES....7

II. EXPERIMENTAL METHODS....9
A. REDUCTION EXPANSION SYNTHESIS-SINTERED METAL....9
1. Shaping and Placing the Sample....14
2. Placing the Compact Sample in the Furnace....17
B. MATERIALS CHARACTERIZATION....19
1. X-ray Diffraction....19
2. Optical Microscope....21
3. Scanning Electron Microscopy/ Energy Dispersive Spectroscopy....22
4. Density Determination Kit....24

III. NICKEL RESULTS....27
A. ACTIVATING THE NICKEL POWDER....27
B. METAL POWDER AND METAL OXIDE POWDER WEIGHT RATIO....30
C. FULL REDUCTION CONFIRMATION....31
D. MORPHOLOGY INVESTIGATION....33
1. Self-supporting Structures between Nickel Particles....33
2. Void Density Investigation.....34
E. SHAPE CREATION....37

IV. IRON RESULTS....45
A. ACTIVATING THE IRON POWDER....45
B. IRON POWDER AND IRON OXIDE POWDER WEIGHT RATIO....46
C. FULL REDUCTION CONFIRMATION....49
D. MORPHOLOGY INVESTIGATION....50
1. Self-supporting Structures between Iron Particles....50
2. Void Density Investigation....53
E. SHAPE CREATION....54

V. CONCLUSION 57
A. ACHIEVEMENTS 57
B. FUTURE WORK 58

LIST OF REFERENCES 59

INITIAL DISTRIBUTION LIST 63

LIST OF FIGURES

Figure 1. AM Market Size and Prediction. Source: [2].....1

Figure 2. Powder Bed Fusion Printer. Source: [5]. 4

Figure 3. Tactical Fabrication Kit at Camp Shelby, Mississippi. Source: [11].....5

Figure 4. Presentation of the First 3D Printed Metal Part on USS *Harry S. Truman*. Source: [13]. 6

Figure 5. Activation of Iron Powder on the Hot plate.....11

Figure 6. Activation of Iron Powder Removed from the Hot Plate 11

Figure 7. Dried Activated Iron Powder.....12

Figure 8. The Metal Oxide was Crushed Primarily.....13

Figure 9. The Activated Metal was Added to the Metal Oxide 13

Figure 10. Mixture of Activated Metal and Metal Oxide.....14

Figure 11. Sample Shape on Grafoil 15

Figure 12. Punctured Grafoil Sheet.....15

Figure 13. Alumina Boat Filled with 0.5 Grams of Urea.....16

Figure 14. Sample on Urea Filled Alumina Boat.....16

Figure 15. Sample Positioned in Quarts Tube.....17

Figure 16. Furnace Setup.....18

Figure 17. Evidence of Thermal Decomposition of Urea at 400 Degrees Celsius 18

Figure 18. X-ray Diffractometer 20

Figure 19. XRD Patter of Pure Nickel 21

Figure 20. Nikon Model Epophot 200 Optical Microscope.....22

Figure 21. SEM with EDS Detector.....23

Figure 22. SEM with EDS Detector. Source: [24]. 24

Figure 23. Ohaus Density Determination Kit....25
Figure 24. XRD Analysis of Ni After Activation Process....28
Figure 25. Activation Chemical Reaction....29
Figure 26. Completed Activation Process....29
Figure 27. Before and After of 50% by Weight Nickel Oxide....31
Figure 28. Self-Supporting Fully Reduced Nickel Bodies....31
Figure 29. Nickel Sample XRD Analysis....32
Figure 30. Nickel Sample after RES-SM Process 300x (left) 2,000 (right) Magnification....34
Figure 31. Nickel Sample after RES-SM Process 10,000x (left) 20,000x (right) Magnification....34
Figure 32. Nickel Raw Optical Image (left) and Binary Image (right) at 20x Magnification....35
Figure 33. Nickel Sample in Ethanol Bath for Density Measurement....36
Figure 34. Mold to Produce Tensile Test Geometry....37
Figure 35. Pre-Bake Nickel Sample with the Mold Removed....38
Figure 36. Nickel Tensile Test Geometry After RES-SM Process....38
Figure 37. HIP Treated Nickel Sample 300x (left), and 2,000x (right) Magnification....40
Figure 38. Non-HIP Treated Nickel Sample 10,000x (left), and HIP Treated Nickel Sample 10,000x (right) Magnification....40
Figure 39. HIP Treated Nickel Raw Image (left), and Binary Image (right) at 20x Magnification....41
Figure 40. Polished HIP Treated Nickel Sample at 1,000x Magnification....41
Figure 41. Polished HIP Treated Nickel Sample EDS Analysis....42
Figure 42. Instron 4507 Tensile Tester....43
Figure 43. Stress-Strain Graph for HIP Treated Nickel Sample....44

Figure 44. Hardness Test taken on Stuers DuraScan 44

Figure 45. XRD Analysis of Iron After Activation Process.....46

Figure 46. Completion of Activation Process 46

Figure 47. 10% FeO Iron Sample (left) and 50% FeO Iron Sample (right).....49

Figure 48. Iron Sample XRD Analysis 50

Figure 49. Micron Sized Iron Powder Out of the Bottle before the RES-SM Process 51

Figure 50. Iron Sample after RES-SM Process 2,000x Magnification (Left), 10,000x Magnification (Right) 52

Figure 51. Iron Sample after RES-SM Process 500x Magnification 52

Figure 52. Iron Raw Optical Image (left) and Binary Image (right) at 20x Magnification.....53

Figure 53. Iron Tensile Test Geometry Shape Before RES-SM Process.....54

Figure 54. Iron Tensile Test Geometry Shape Before RES-SM Process.....55

THIS PAGE INTENTIONALLY LEFT BLANK

LIST OF TABLES

Table 1. Weight Ratios Experimental Results for Nickel.....30

Table 2. Density Measurement Results.....36

Table 3. Density Measurement Results for HIP Treated Nickel.....42

Table 4. Weight Ratios Experimental Results for Iron.....47

Table 5. Density Measurement Results for Iron Sample.....54

THIS PAGE INTENTIONALLY LEFT BLANK

LIST OF ACRONYMS AND ABBREVIATIONS

AM	additive manufacturing
3D	three-dimensional
P-AM	plastic additive manufacturing
M-AM	metal additive manufacturing
RES-SM	reduction expansion synthesis of sintered metals
TACFAB	tactical fabrication
USN	United States Navy
NPS	Naval Postgraduate School
RES	reduction expansion synthesis
XRD	X-Ray Diffraction
SEM	scanning electron microscopy
EDS	energy dispersive x-ray spectroscopy
SCCM	standard cubic centimeters per minute
SE	secondary electrons
eV	electron volts
nA	nanoamperes
Ni	Nickel
NiO	Nickel Oxide
Fe	Iron
FeO	Iron Oxide
AIP	American Isostatic Presses
MPa	mega Pascal

THIS PAGE INTENTIONALLY LEFT BLANK

EXECUTIVE SUMMARY

A new and novel method of metal additive manufacturing was discovered and explored. The Reduction Expansion Synthesis-Sintered Metal (RES-SM) process proved to be able to produce a sintered metal body at hundreds of degrees below the metal melting temperature. The RES-SM process was tested on nickel samples and iron samples. The precursor to the nickel metallic part was a mixture of activated nickel particles and nickel oxide particles. The precursor to the iron metallic part was a mixture of activated iron particles and iron oxide particles. The RES-SM process involves exposing the activated metal and metal oxide to reducing radical species produced by the thermal decomposition of urea or other organic room temperature solids. In the research performed, the highest required temperature was 900 degrees Celsius with a duration of 1200 seconds. An inert atmosphere was created with flowing nitrogen gas. Different characterizing techniques were employed to verify the creation of self-supporting structures between the metal particles. Scanning electron microscopy confirmed the creation of necks between the metal particles. The RES-SM process creates hard and fully self-supporting samples that are able to be handled. However, the samples do not have the same physical properties (density, hardness, ductility, and electrical/thermal conductivity) as a metal piece of similar size produced from the nucleation of liquid metal. The samples created after the RES-SM process are considered ‘“green”‘ metal parts and require post-processing to fully densify.

The researched concluded that the powder could be shaped before being placed in the furnace. The shapes could be casted using 3D printed plastic shapes. The powder held its shape during the RES-SM process and therefore could be maneuvered and handled. The sample after the RES-SM process was not fully densified and did not have the same physical characteristics as pure metal with respect to tensile strength. The nickel samples were able to produce clean and sharp shapes. The iron samples were not able to produce clean shapes which is attributed to the casting process.

The optimal weight ratios of metal powder and metal oxide powder were determined experimentally. The optimal weight ratio for the iron samples was ten percent

iron oxide. The optimal weight ratio for the nickel samples was fifty percent nickel oxide. The experiments were carried out using 0.5 grams of urea.

The RES-SM process produced sintered particles at a temperature of 900 degrees Celsius which is hundreds of degrees below the melting temperature of iron and nickel. The particles were held together by self-supporting structures in the form of necks between the particles. There was still evidence of voids between the particles and the sample was not fully densified.

It was determined experimentally that the size of the metal powders affected the outcome of the RES-SM process. More successful trials were accomplished using a finer metal powder, typically a powder with a particle size less than six microns. The particle size in the powder affected the oxidation process and how many self-supporting structures formed in the RES-SM process.

ACKNOWLEDGMENTS

I would like to thank LT Zachary Daniels, who provided training and assistance for many of the experiments conducted in my thesis. Your experience and knowledge were an incredible resource.

I would like to thank Dr. Claudia Luhrs for assisting me with my experiments in the lab. You always had an answer for me when I had a question, and you were willing to help me in any way you could.

I would like to thank Dr. Troy Ansell for help in training me on the different characterization techniques throughout my research, and for always being available to answer questions when I needed help.

Finally, I would like to thank my thesis advisor, Dr. Jonathan Phillips, for guiding me through my research and providing direction and supervision. Your expertise and willingness to try the unknown helped me to work harder every day and reach my goals. I greatly enjoyed the mentorship you provided and the insightful conversations we had about my research. I am thankful for your dedication to seeing your students succeed and willingness to help in every way you can.

THIS PAGE INTENTIONALLY LEFT BLANK

I. INTRODUCTION

Additive manufacturing (AM), also known as three-dimensional (3D) printing, rapid prototyping, layered manufacturing, and solid freeform fabrication [1], is widely employed, and its use is growing. In 2018, the global additive manufacturing market, which includes the software, materials and services, generated $9.3 billion in revenues, a growth of 18% from 2017 [2]. It is projected to continue growing to $41.59 billion in revenues by 2027, as presented in Figure 1 [2]. Although growth is impressive, best projections show AM will continue to produce only a very small portion for the foreseeable future, less than 0.1%, of the gross sales of commercial manufactured goods, estimated revenue $35 trillion, worldwide, in 2017. To make a significant impact, AM must be faster, produce better parts, and there must be breakthroughs to increase the very limited pallet of materials that can be used to create parts at a reasonable cost with AM.

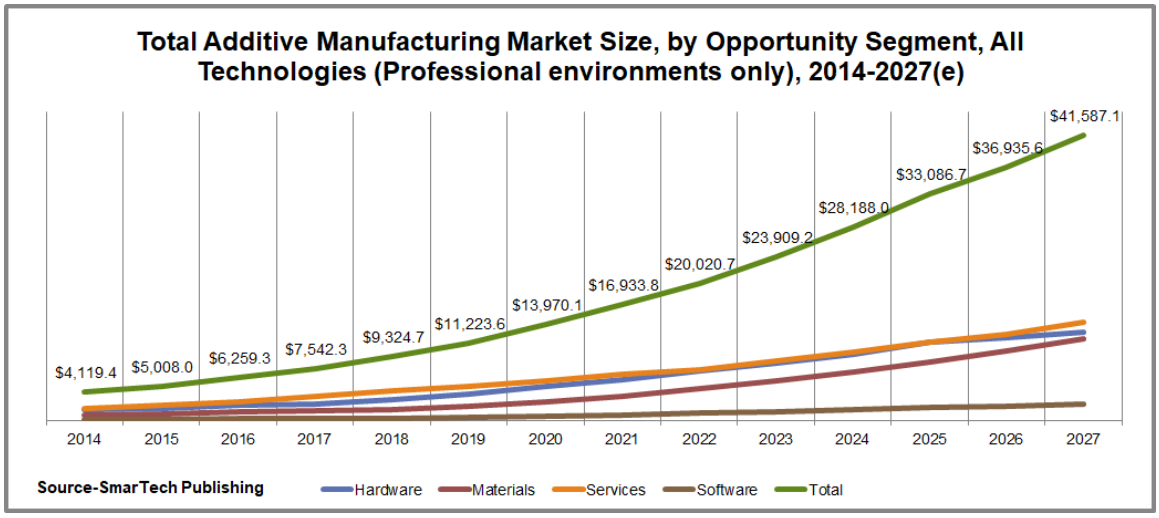

Figure 1. AM Market Size and Prediction. Source: [2].

AM is a technology with charisma! It appears to have inherent advantages, hence significant investment to improve the technology is anticipated [3]. Contrasted with subtractive manufacturing, AM does not require cutting tools or coolants, and there is no wasted material in the manufacturing process. AM has numerous advantageous qualities,

including geometric flexibility, short lead times, superior design, large size manufacturing capabilities, and overall savings in costs [3].

AM is best understood as two very different technologies at very different levels of development; Plastic additive manufacturing (P-AM) and Metal additive manufacturing (M-AM). Currently thermoplastics are the most common material used in AM. P-AM is well understood and requires little investment. Reliable tools for small scale manufacture could cost less than $1000, and it can be successfully employed with minimal training. There are limits to finished products with regard to physical properties due to the limits of the construction material, plastic. Metal AM, required to build most ship parts and other military grade hardware, is not widely used. It is very expensive, even tools capable of slowing (ca. >1 hr) making small parts (ca.1 in^3) cost of the order of six figures. Also, these tools requires significant training to master and typical tools are tuned to a specific metal or alloy.

At NPS we are undertaking several efforts to develop alternative/novel "metal additive manufacturing" strategies. In this work we introduce a "hybrid" technology, reduction expansion synthesis of sintered metals (RES-SM) for metal additive manufacturing. RES-SM employs inexpensive Plastic AM, novel chemistry, and a variant on traditional casting technology. The total facility investment, a furnace and a low-cost 3D printer, is about 1% that of current M-AM tools. This hybrid method is still "M-AM" by the broad definition: no material is removed in the creation of a designed shape. It is also "smart" technology in that it employs various approaches synergistically to create, inexpensively, the same type of part created using current M-AM tools.

A. CURRENT M-AM TECHNOLOGIES

Powder bed fusion is the most common metal additive manufacturing technique. Powder bed fusion originated from selective laser sintering [3]. The basis of powder bed fusion consists of three fundamental steps: (i) a thin layer of metal powder is placed on the building platform, (ii) a high power laser is focused on the cross section causing the metal particles to fuse together, and (iii) after the lasering of the thin layer the platform lowers and a new thin layer of metal powder is spread over the cross section [4]. It is notable that

operation of a typical M-AM requires extensive training, and a physically stable, specifically non-shipboard, environment.

Powder bed fusion can be used to manufacture complex parts with intricate geometries that traditional manufacturing methods are unable to produce. M-AM printed parts can be topologically optimized to minimize weight. A wide variety of metals can be used in M-AM, including super alloys that have excellent physical properties. However, some of the major disadvantages of current metal additive manufacturing processes include, surface finish, and size limitations and tool cost. Because sintering and cooling is taking place on every thin level (layer thickness between 20 and 50 microns), the printing time for a metal part is, greater than 48 hours in some cases [4], [5]. For most metal additive manufactured parts the surface finish is poor, that is “smooth” only on the order of the primary particle size used in the manufacturing (ca 20 microns) and requires post processing finishing. M-AM surface finish is considered very rough and some of the post-processing surface finish that are required are disk finishing, high-energy centrifuge and stream finishing [6]. These surface finishing techniques increase the cost of production and production time. Current technology limits the size of metal additive manufactured parts to the size of the metal 3D printer, presented in Figure 2. The Ultimake 3 Extended 3D printer has maximum print size capabilities of 215 x 215 x 300 mm (xyz) [7]. Also, although many metals can be used, the tools require extensive reconfiguration (ca. 1 day by expert) for each metal. Common metal powders and metal alloy powders used in metal additive manufacturing are: titanium (Ti-6Al-4V, ELI titanium, and Cp titanium), aluminum (Al-Si-Mg, and 6061), super alloys (IN625, IN718, and Stellite), stainless steel (316, 420, and 347), and refractory (MoRe, Ta-W, Co-Cr, and Alumina) [3]. One of the most advanced commercial metal additive manufacturing printer is the Skiaky Electron Beam Additive Manufacturing (EBAM) System. The EBAM systems have different sized printers with different capabilities [8]. The Skiaky EBAM has a maximum build size of $5{,}791 \times 1219 \times 1219$ mm and the price of a printer that large is generally over one million dollars [9].

Figure 2. Powder Bed Fusion Printer. Source: [5].

Another method to creating manufactured 3D metal parts is a hybrid of casting and P-AM. This hybrid method is limited to metals with low melting temperatures. Such metals like indium and tin are generally not strong enough for structural elements. The general process involves pouring molten metal into a 3D printed plastic mold. Fusible alloys are metals or alloys that have relatively low melting points typically less than 183 degrees Celsius [10]. Common fusible alloys are bismuth, lead, tin, cadmium, and indium [10]. As long as the melting temperature is less than the melting temperature of the plastic mold the casting process can successfully be accomplished.

There are many disadvantages to current low temperature casting methods particularly physical properties such as strength. Other issues include surface finish, the toxic character of many of the low fusion temperature metals and alloys. Indeed, the available metals generate noxious vapors when melted.

B. METAL ADDITIVE MANUFACTURING NEEDS IN UNITED STATES NAVY

AM technologies is increasingly employed by the United States Navy and by U.S. space programs. In February of 2019 it was reported that the Seabees from Naval Mobile

Construction Battalion 133 deployed for the first time with P-AM capabilities [11]. The "Tactical Fabrication (TACFAB) Kits" contained laptops, computers, 3-D scanners, printers, and all the required software, presented in Figure 3 [11]. Wait times for a replacement parts while in deployment can be between 30 and 90 days [11]. However, with the ability to print the needed part on the spot the only wait time is the time to draw the part in CAD and print it out. The TACFAB Kits can produce fully functioning, certified, small plastic parts, and can save the Defense Department tens of thousands of dollars on replacement parts. In contrast to success with P-AM, the U.S. Navy is still in the evaluation phase of potentially viable M-AM for forward deployment.

Figure 3. Tactical Fabrication Kit at Camp Shelby, Mississippi. Source: [11].

Maximizing ship utility is one reason for USN interest in AM. In theory, submarines with shipboard tools for the manufacture of replacement plastic and metal parts would have reduced time in port, and concomitantly maximum time on mission. It is estimated that the ability to 3D print both metal and plastic replacement parts while on mission would save tens of thousands of dollars per replacement part [11]. In October of 2018 it was reported that the U.S. Navy's Naval Sea Systems Command had approved the

replacement of a metal part with a part created by a metal 3D printer [12]. The 3D printed part is a steam system component, presented in Figure 4 [12]. The 3D printed part had to go through numerous tests to ensure the quality of the part. Some of the test were shock, vibration, material, welding, hydrostatic, and operational steam [12]. These tests were conducted at different temperatures, pressures, and humidity to ensure the 3D printed part satisfied the required standards in different environments. The part is currently installed on the carrier USS *Harry S. Truman* (CVN-75) for a one-year evaluation trial [12].

Figure 4. Presentation of the First 3D Printed Metal Part on USS *Harry S. Truman*. Source: [13].

C. REDUCTION EXPANSION SYNTHESIS

The reduction expansion synthesis (RES) is a novel method invented by NPS Professors Luhrs and Phillips. There are two fundamental and unique steps to the RES process: (i) a molecular, oxidized or partially oxidized metal is put in an atmosphere with a chemical reducing agent, generally urea, that releases reducing agents once it starts to thermally decompose, and (ii) the atmosphere is heated above the thermal decomposition temperature of the reducing agent [14]. The RES process has been used in multiple applications: creating graphene from graphite oxide [15], doping graphene with other metals [16], the reduction of hydroxides to form metal particles [17], the creation of anti-

corrosion metal coatings [18], creating uniquely stable battery [19] and fuel cell electrodes [19], and other studies.

An exemplary use of the RES process is the solid-state reduction of metal oxides [20]. In the study the metal oxide (NiO) precursor was physically mixed with urea and placed in an alumina boat. The alumina boat was placed in the center of a quartz tube with nitrogen gas flowing through. The quartz tube was maneuvered into the furnace and after heating the sample was examined. The study concluded that the nickel oxide was fully reduced and only nickel powder remained. The nickel particles were on the order of 1 or 2 micron in diameter. The study proved that the RES process was capable of reducing metal oxides and that the RES process could have further application to metal additive manufacturing.

Notably, this process is easily scaled to very large size, and the metal particles produced are far smaller (ca. ~10,000 x smaller) than those made using “atomization” (REFS), the present standard for metal particle production. The availability of sub-micron particles might eliminate the post-process polish required for metal parts generated with M-AM.

D. OBJECTIVES

The goal of this research was to test a simple hypothesis regarding a means to create a green metal body of designed shape faster, and at lower cost than possible using standard M-AM. The hypothesis was that a form of RES can be used to make a metallic “green” body. Specifically: A particular shape created by loosely compressing to a homogenous mixture of metal and metal oxide particles, then exposed in an inert atmosphere to the by-products of thermal urea decomposition, will form a solid metallic green body in a few minutes. All work in this thesis was directed to this goal, and the outcome was a clear demonstration that the hypothesis is correct.

The shapes were made by casting the powders into different shapes using 3D generated molds. These shapes were then placed in an ordinary laboratory tube furnace above a small bed of urea, air removed, then heated to about 900 C for less than 10 minutes. Post process examination revealed that relatively high density (ca 90%) green, all metal,

bodies that retained the “shape,” but not the size, of the original mold were generated. At the end of the process, hot isostatic pressing (HIP), the same post process used on most commercially generated M-AM green bodies, was applied and this created ~100% dense parts.

Thus this research confirmed every element of the hypothesis. First, it is possible to sinter together metal powders at hundreds of degrees below their melting points using the RES-SM process. Thus, an inexpensive laboratory furnace, not a complex high-powered laser, is the only energy source required. Second, it was clearly demonstrated that metal powders can be casted into specific shapes using the RES-SM process. No metal is removed; thus it can be referred to a type of AM. The outcome of this work suggests it is possible to develop a commercial version of RES-SM that would allow rapid, inexpensive, simple fabrication of metal parts. This outcome would likely directly influence the way the United States Navy replaces metal parts on its ships and submarines where weight and space are limited.

Chapter I provides an introduction to AM technologies that are applicable to this thesis and background information about the RES method. Chapter II provides information on the experimental methods used for the RES-SM fabrication process and the material characterization. Chapter III outlines the results achieved and the different conditions that produced optimal results. Lastly, Chapter IV presents the conclusion of this research outlining the major accomplishments and recommendations for further studies.

II. EXPERIMENTAL METHODS

The following sections in this chapter describe the synthesis process, creation and characterization techniques for classifying the sample. The synthesis process was done chiefly through the Reduction Expansion Synthesis-Sintered Metal (RES-SM) method. The RES-SM technique is hypothesized, during thermal treatment far below metal melting temperature, to reduce micron scale metal oxide particles, producing mobile metal atoms that diffuse and attach to existing metal crystals. It is further postulated this process leads to the formation of necks between metal particles, hence the generation of macroscopic metal green bodies. Finally, it is hypothesized that the macroscopic metal parts that form during the process remain true to the shape, but not the size, of the original metal/metal oxide compact. Thus, it is concluded that the process permits a form of low temperature metal casting.

Experiments to test these hypotheses were conducted using nickel/nickel oxide and iron/iron oxide. Characterization at various points of the synthesis were conducted using X-Ray Diffraction (XRD), Optical Microscopy, density measurement, Scanning Electron Microscopy (SEM), and Energy Dispersive X-Ray Spectroscopy (EDS). The results were strongly supportive of the hypothesis.

A. REDUCTION EXPANSION SYNTHESIS-SINTERED METAL

The RES-Sintered Metal (RES-SM) method was developed by Dr. Phillips. It is one of a number of RES based processes. In all RES processes a reductive-expansion agent is decomposed thermally in an inert atmosphere to produce radicals. Urea is an example of a reductive-expansion agent. The thermal decomposition of urea releases gases, such as CO and NHx groups that are believed to reduce oxides in the target object, leaving reduced metal at temperatures well below the melting temperature of the material.

The RES-SM method is a novel variation on the RES process. It consist of three different processes: making a compact sample of metal powder, shaping the compact sample and placing the compact sample in the furnace along with the reductant agent (urea), and heating the compact sample and reductant material for a short time at a

temperature hundreds of degrees Celsius below the melting temperature of the compact sample.

The basic chemistry of the RES-SM process is similar to that of other RES processes. The particular RES process originally designed for this work, RES-SM, was very simple. First, urea in a bed below the metal/metal oxide compact is thermally decomposed at about 900C in an inert atmosphere. The decomposition was intended to produce radical species that would diffuse up to and interact with the oxide particles in the metal powder compacts. Specifically, the radicals react with the metal oxide to create volatile oxides, like carbon dioxide, leaving behind the reduced metal atoms. It was postulated the metal atoms produced by this process would diffuse to existing metal crystals, and add to them. Eventually this would lead to metal necks connecting all the metal particles (green body) originally present in the compact, and the complete reduction of all metal oxide initially present.

The process finally adopted was nearly identical to that originally designed (above) but one particular pre-heating step was added. It was found to improve the final green body strength that the metal particles in the compact should be "activated" prior to forming the metal/metal oxide compact. The activation process was done by placing the metal powder, nickel (Sigma-Aldrich 5 µm, 99.7% purity) or iron (5 µm, 99.5% purity) in a ten mL bath of 30% Hydrogen Peroxide and then heating it on a hot plate to a temperature of 100 degrees Celsius for five minutes as shown in Figure 5. The bubbles forming indicate that a reaction is taking place. The sample was removed from the hotplate and allowed to sit for three minutes until the reaction was completed and the bubbling concluded, illustrated in Figure 6. When the reaction concluded the sample was flushed with distilled water, decanted, and then dried until only the powder remained, presented in Figure 7. Drying the sample consisted of placing the sample on the hot plate and evaporating all of the liquid until only the activated metal powder remained.

The activation clearly only modifies the surface of the metal particles. Neither XRD nor EDX performed in the SEM was able to detect any change in the particles. For example, no oxide was detected before or after activation. It is postulated that the primary role of the

activation is surface cleaning. That is, activation removes carbonaceous material commonly found on all surfaces, creating a clean surface for the RES-SM process.

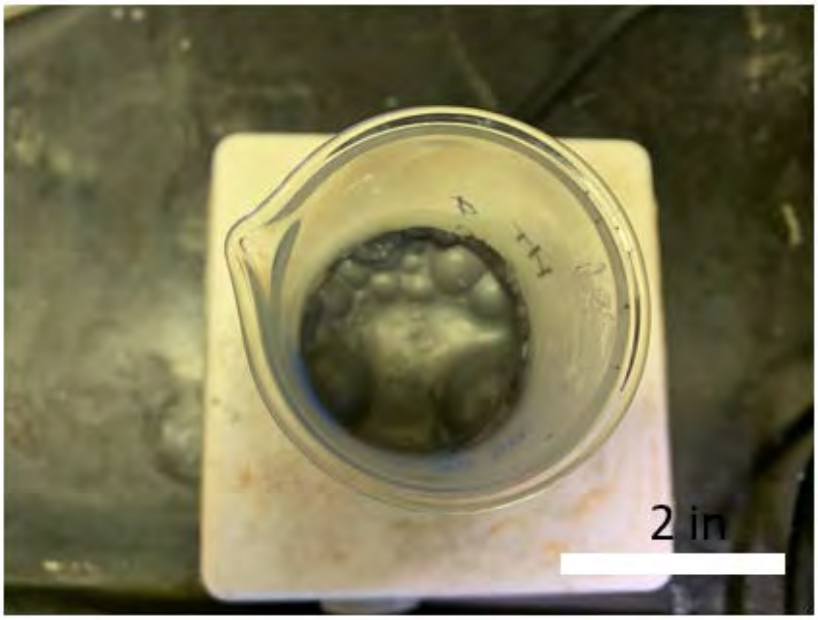

Figure 5. Activation of Iron Powder on the Hot plate

Figure 6. Activation of Iron Powder Removed from the Hot Plate

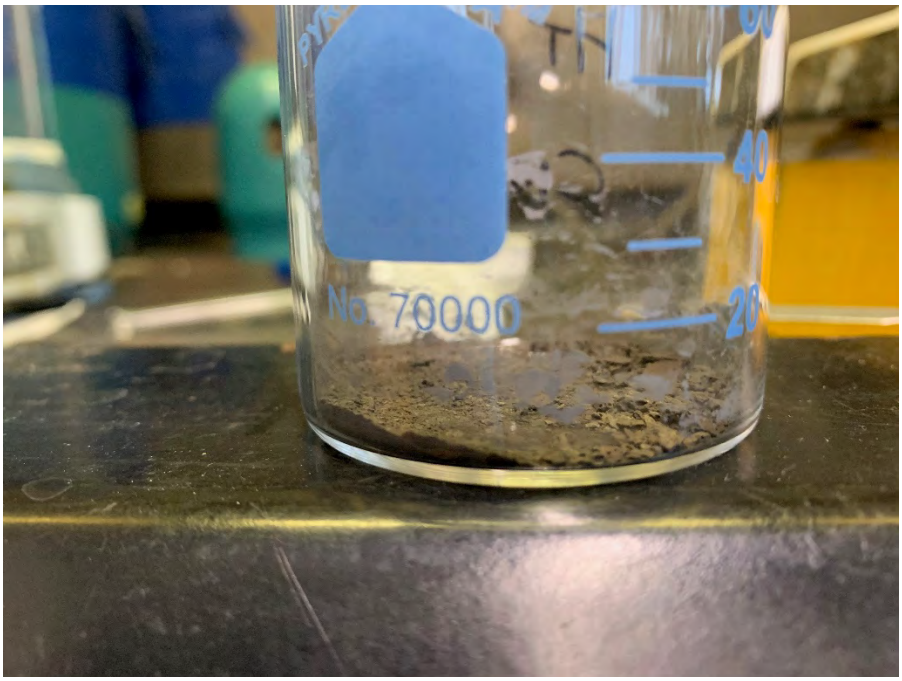

Figure 7. Dried Activated Iron Powder

Creating the physical samples consisted of mixing a micron sized activated metal powder with a micron sized metal oxide powder of the original metal powder. The metal oxide was crushed primarily using a mortar and pestle to allow for better mixing with the metal powder, shown in Figure 8. The metal oxides used in the experiments were nickel(II) oxide (Sigma-Aldrich) and iron(III) oxide (Sigma-Aldrich). The mixtures were created by physically grinding the metal powder and metal oxide powder together with a mortar and pestle, presented in Figure 9 and 10. The powders were mixed together for three minutes. The weight ratio of the metal powder to metal oxide powder was varied and tested over a wide range. An optimal weight ratio was determined through tested trials and repeatability. For nickel samples, 2 grams of micron sized nickel powder was activated and then mixed with a pre-determined amount of nickel oxide using a mortar and pestle. For the Iron samples, 2 grams of micron sized iron powder was activated and then mixed with a pre-determined amount of iron oxide using a mortar and pestle.

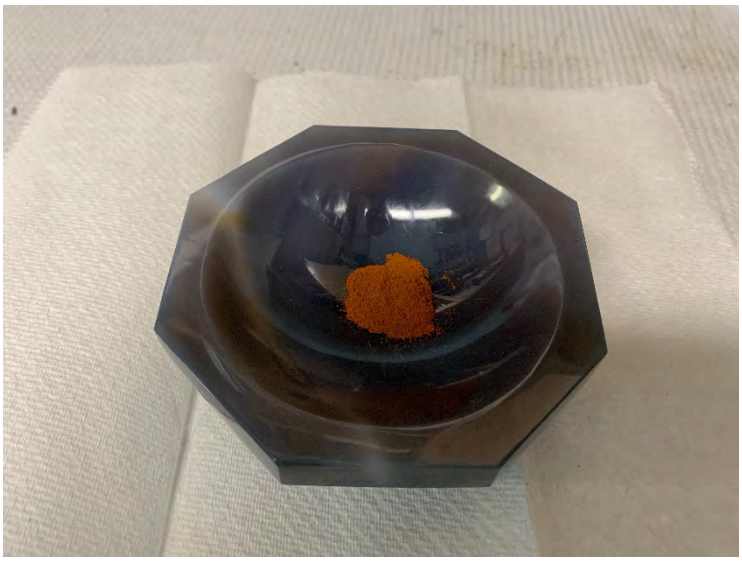

Figure 8. The Metal Oxide was Crushed Primarily

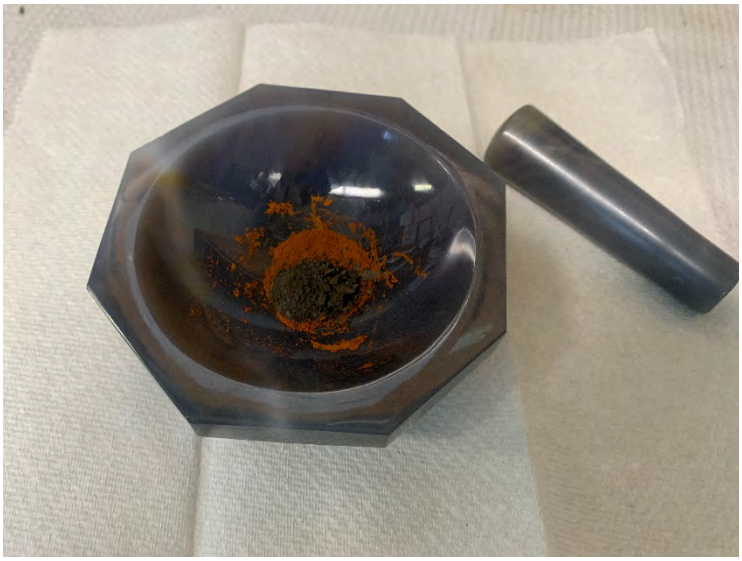

Figure 9. The Activated Metal was Added to the Metal Oxide

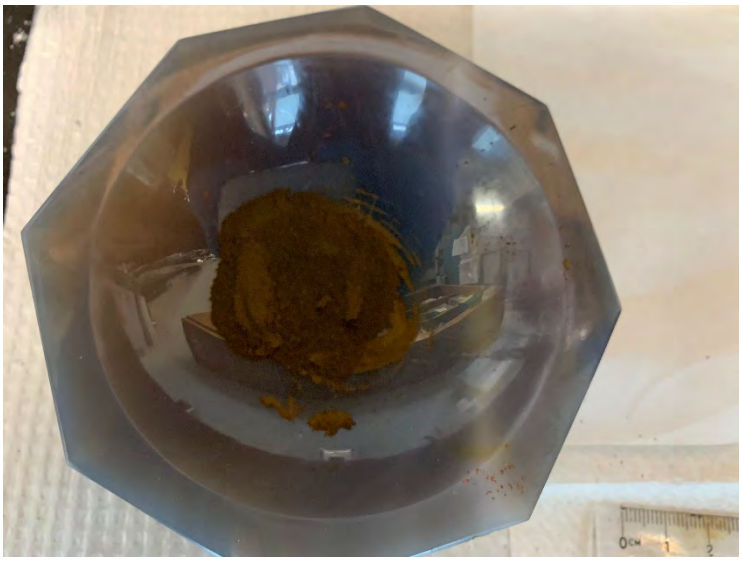

Figure 10. Mixture of Activated Metal and Metal Oxide

1. Shaping and Placing the Sample

Originally the sample shape was created by roughly shaping the powder precursor by hand. The metal and metal oxide mix was shaped into a rectangular shape that was approximately 4 cm x 1 cm x 2 mm deep, illustrated in Figure 11. The shape was created on top of a rectangular piece of Grafoil 5.7 cm x 1 cm. The Grafoil was punctured to create many pin holes, presented in Figure 12. The pin holes were necessary to promote the flow of the reducing radicals from the urea to the sample. The Grafoil with the sample was placed upon an alumina boat that was filled with 0.5 grams of urea (Figure 13). The metal powder sample was position on the alumina boat at 5 mm above the urea, illustrated in Figure 14. As experimental success was found, molds were used to shape the samples into specific shapes.

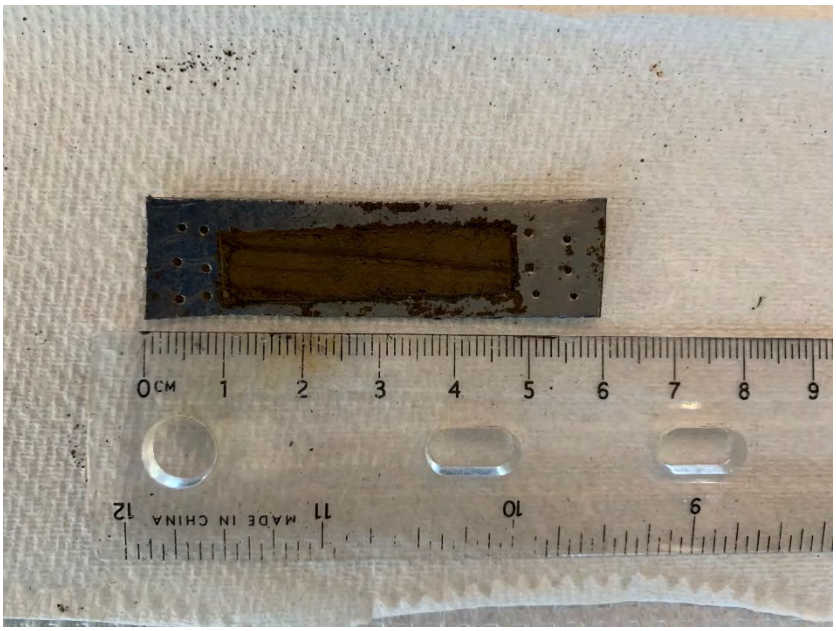

Figure 11. Sample Shape on Grafoil

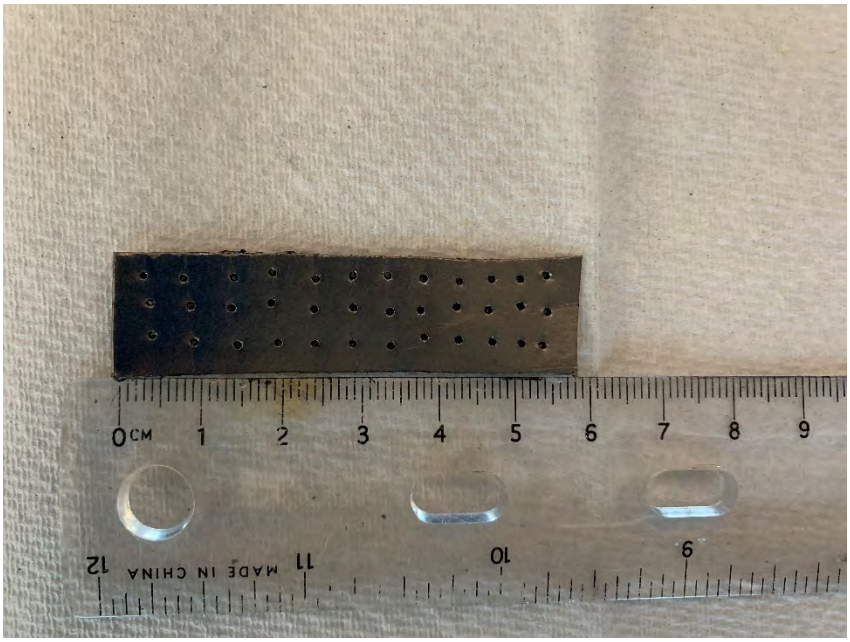

Figure 12. Punctured Grafoil Sheet

Figure 13. Alumina Boat Filled with 0.5 Grams of Urea

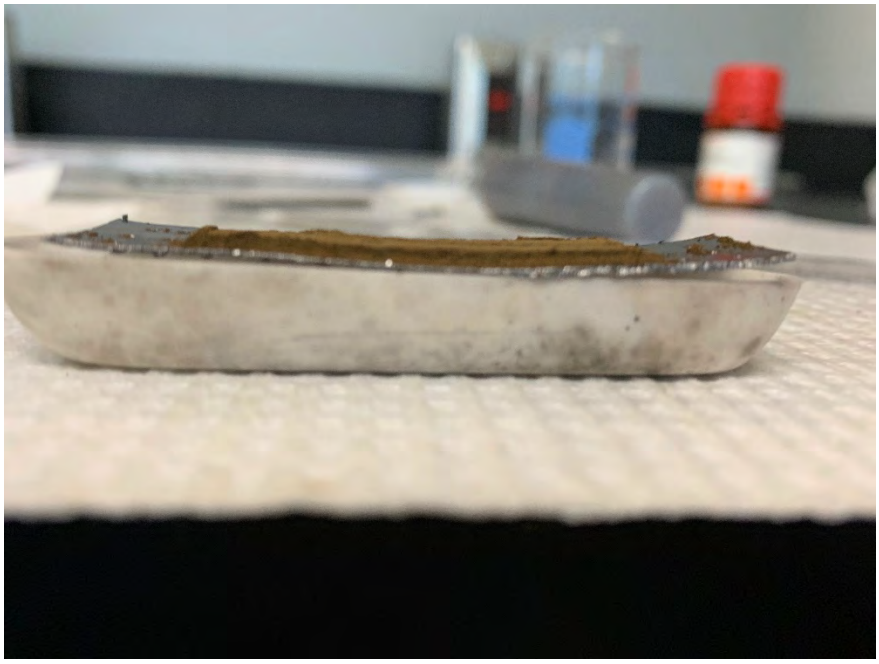

Figure 14. Sample on Urea Filled Alumina Boat

2. Placing the Compact Sample in the Furnace

In order for the sample to be heated in the furnace in an inert atmosphere, it needed to be placed in a quartz tube. The sample was placed in a 50 cm x 2.5 cm diameter quartz tube, shown in Figure 15. The quartz tube allowed the creation of an inert atmosphere. The quartz tube with the sample inside was flushed with nitrogen gas flowing at 50 standard cubic centimeters per minute (SCCM) for 600 seconds. The flow rate of the nitrogen gas was reduced to 10 SCCM, and the quartz tube with the sample was positioned in in the furnace, presented in Figure 16. The furnace was heated to 900 degrees Celsius in 600 seconds and then maintained that temperature for 1200 seconds. The thermal decomposition of urea takes place at 400 degrees Celsius and is made evident by the quartz tube filling with gas, illustrated in Figure 17. The quartz tube was quickly removed from the furnace and the flow rate of the nitrogen gas was increased to 50 SCCM. The sintered sample inside the quartz tube was allowed to cool at ambient temperature for 20 minutes.

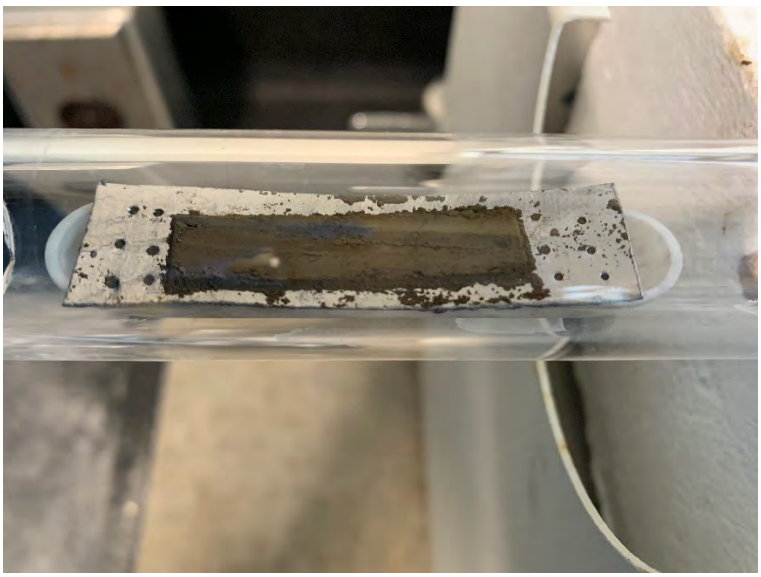

Figure 15. Sample Positioned in Quarts Tube

Figure 16. Furnace Setup

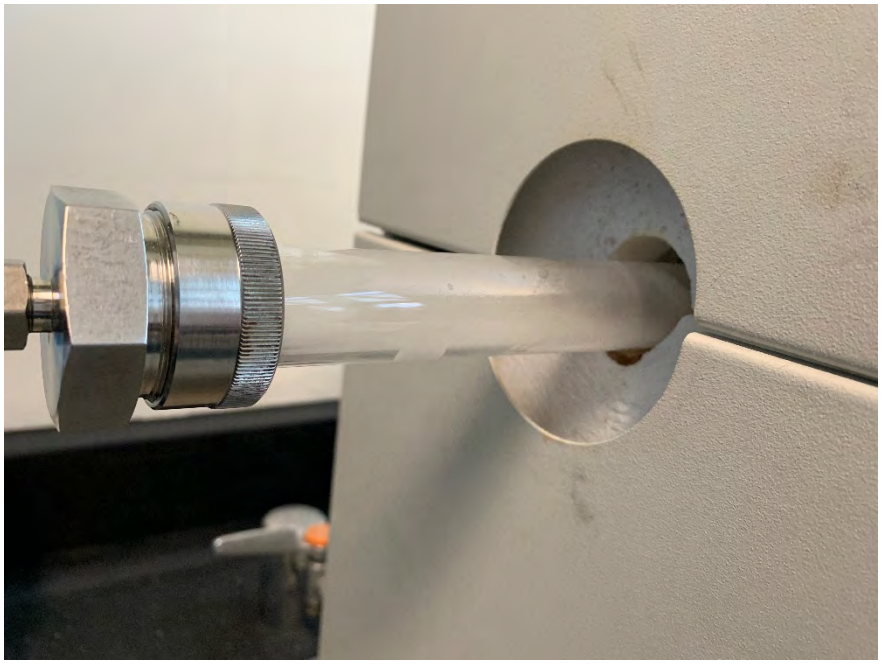

Figure 17. Evidence of Thermal Decomposition of Urea at 400 Degrees Celsius

B. MATERIALS CHARACTERIZATION

In order to characterize and determine the degree of success of different trials at the microstructure level, various characterization techniques were employed. The four primary characterization methods used in this thesis were XRD, optical microscope, SEM-EDS, and a density determination kit.

1. X-ray Diffraction

X-ray Diffraction (XRD) analysis was used to characterize the sample at different stages throughout the manufacturing process. All samples were examined in the Rigaku Miniflex 600 X-ray Diffractometer, presented in Figure 18. The instrument takes advantage of the elastic scattering of X-rays to provide different information about the sample being investigated [20]. The instrument is capable of classifying a crystalline unknown material, detecting changes in the peak positions due to residual stress, providing information on lattice structure, geometry, constants, and direction [21]. The instrument can be used to determine the purity of a sample and if there have been any crystalline contaminates. One of the limitations of this tool is that it requires that the sample be crushed into powder form. The primary use of this instrument for this research is to classify materials and validate the absence of crystalline contaminates.

Figure 18. X-ray Diffractometer

X-rays are produced in the X-ray diffractometer. Electromagnetic radiation with a wavelength between 0.01 and 100 angstroms is classified as an X-ray [20]. Typically, the X-ray diffractometer produces X-rays at 1 angstrom which corresponds to the interatomic spacing in crystals [20]. The diffraction that occurs when the incident X-rays interact with the sample can be described using Bragg's Law.

$$n\lambda = 2dsin\theta \quad (1)$$

In Equation 1 *n* is the integer number, *d* is the distance between crystal planes also known as d-spacing, λ is the wavelength of the incident X-rays, θ is the Bragg angle or the diffraction angle that is observed at the diffraction peaks [20].

XRD is convenient to use in materials classification because the instrument provides reliable analysis and the sample preparation is relatively easy to perform. The sample preparation consisted of crushing a small portion of the sample using a mortar and pestle until the sample was a fine powder, compacting and positioning the fine powder on the sample carriage, and mounting the carriage containing the sample in the XRD. The X-Ray diffractometer analysis conditions were set to 20 kV, and 2 mA using a copper X-ray

source of 1.54 angstrom. The sample was tilted from 10 degrees to 120 degrees (2θ) at a speed of 3 degrees per minute. Figure 19 shows an example of a captured spectrum. The XRD analysis is a non-destructive analysis, so after the analysis the samples were removed and stowed for further testing and characterization.

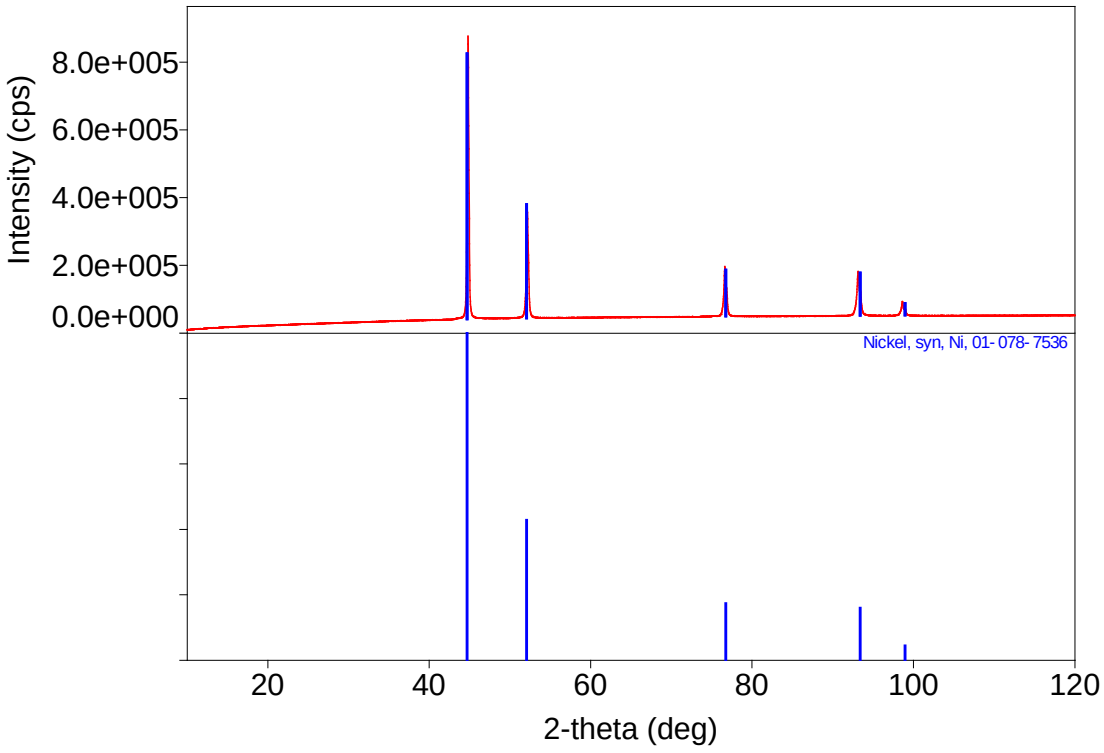

Figure 19. XRD Patter of Pure Nickel

2. Optical Microscope

Samples were observed and analyzed using optical microscopy on the Nikon Model Epiphot 200, shown if Figure 20. Optical microscopy was used to study the porosity of the samples. An optical microscope uses an illuminator to transmit visible light through a condenser and the sample stage where the specimen is located [22]. The condenser focuses the light from the source to investigate tiny spots on the specimen. The Nikon Model Epihphot 200 was equipped with a camera to display the imaging on a computer screen.

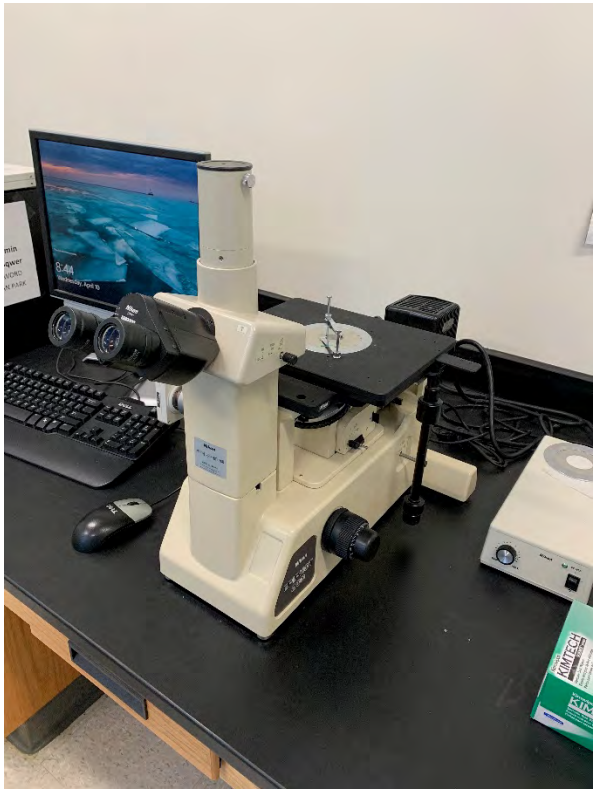

Figure 20. Nikon Model Epophot 200 Optical Microscope

3. Scanning Electron Microscopy/ Energy Dispersive Spectroscopy

Microscopic structures and characteristics were investigated using scanning electron microscopy (SEM) with the SEM Ziess Neon 40 FESEM equipped with energy dispersive spectroscopy (EDS) detector, presented in Figure 21. SEM is the most common type of electron microscope [23]. The SEM image is created by a focused electron beam that travels over the surface area of the sample. SEM provides surface imaging and is non-destructive. The electrons from the electron beam interact with the sample. The SEM is able to generate images from interactions between the electrons and the sample.

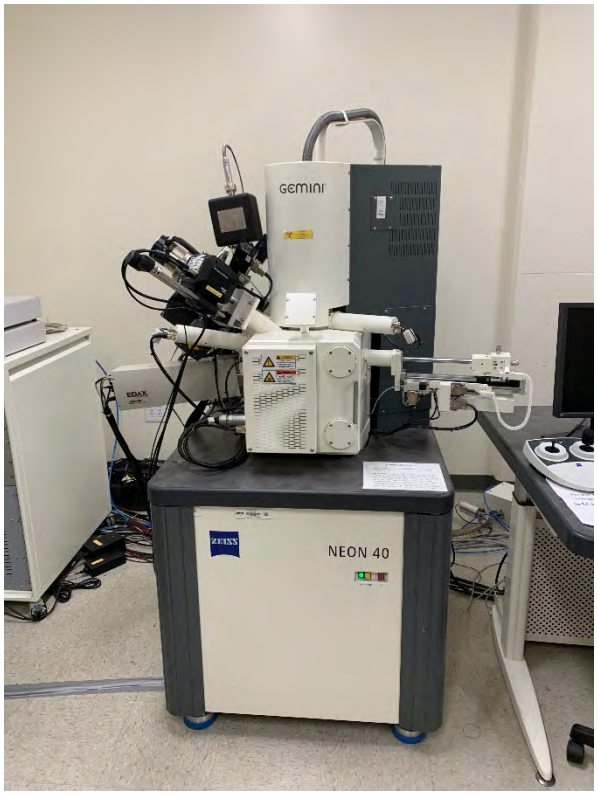

Figure 21. SEM with EDS Detector

Electron microscopes can provide information about the topography, morphology, composition, and structure of the specimen being examined. Electron microscopes use different electron interactions with the sample to produce images, but for this study Secondary Electrons (SE), were the primary interaction used for imaging. SE are generated from the collision between the electrons generated from the microscope and the outer electrons, or free electrons, on the sample. The electrons, generated from the microscope, transfer their kinetic energy to the free electrons when they collide. When the free electron has enough energy to overcome the attractive force of the nuclei it escapes [23]. These escaping electrons are known as secondary electrons, depicted in Figure 22. SE are low energy electrons with energies less than 50eV [23].

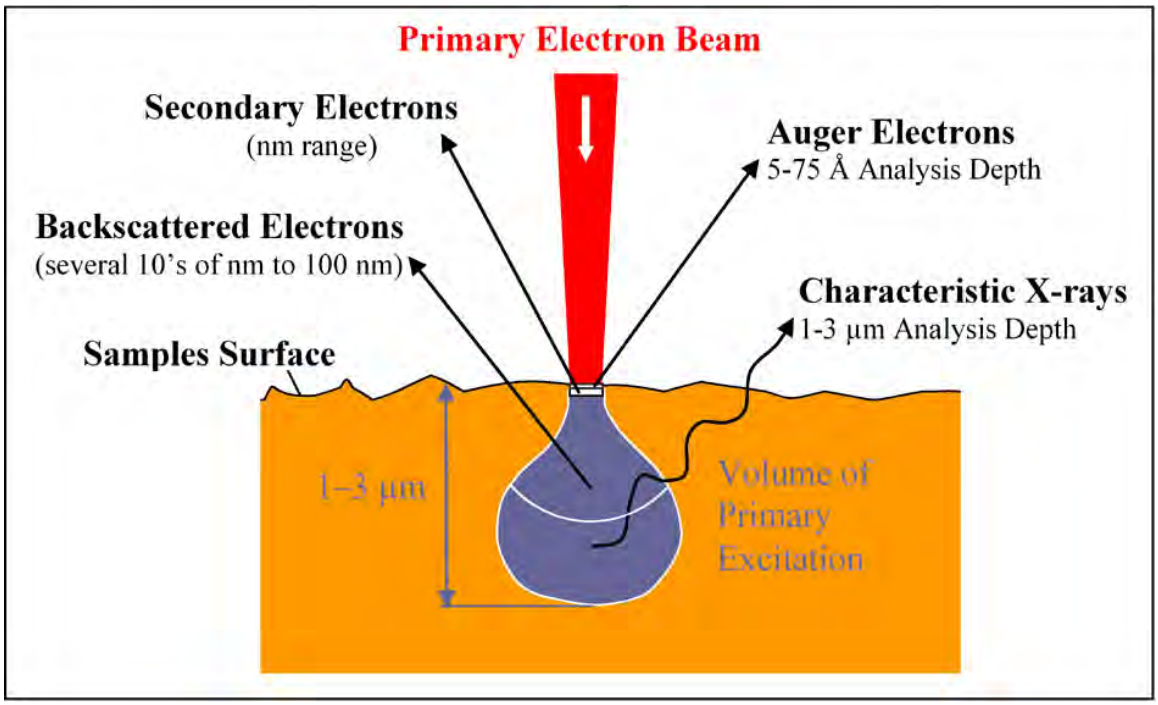

Figure 22. SEM with EDS Detector. Source: [24].

The SEM Ziess Neon 40 FESEM is equipped with an EDS detector. EDS uses the emission of characteristic X-rays (Figure 22) to classify the presence and relative amounts of individual elements in the area of the sample under investigation. During EDS analysis, the SEM was set to an energy of 20keV and a current of 1.32 nA.

4. Density Determination Kit

The Ohaus density determination kit uses the buoyancy method to make density measurements of the sample. Archimedes principle states that the weight of displaced liquid by an object is equal to the buoyancy force that the object is subject to. Using the Ohaus density determination kit involves placing a sample under investigation on a weigh pan that is connected to a scale and is submerged in a liquid bath, presented in Figure 23. For these analysis ethanol was used as the liquid bath. Using the weight of the displaced ethanol, the density of ethanol at the temperature that the measurements are being made, and the dry weight of the sample, the density of the sample can be determined.

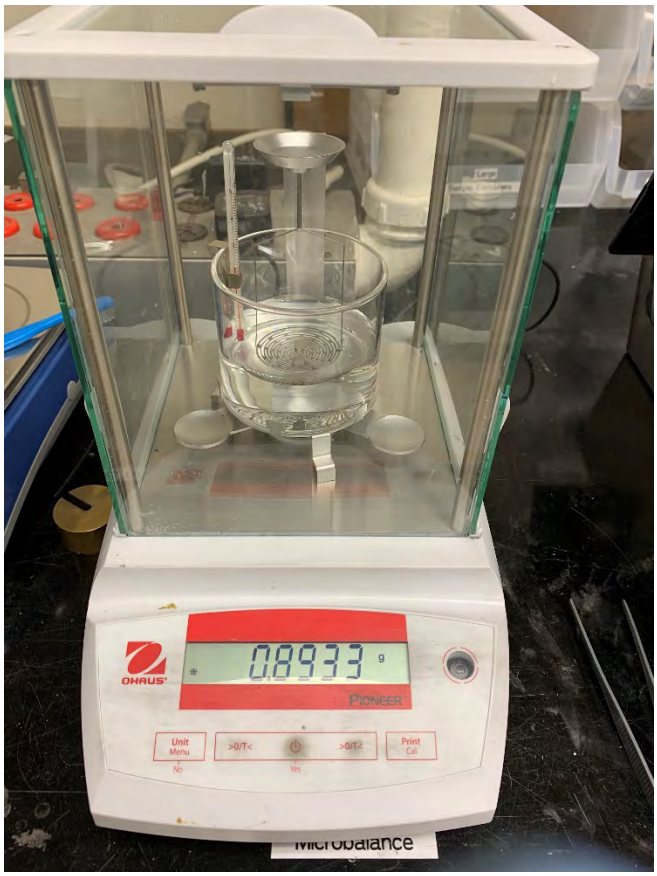

Figure 23. Ohaus Density Determination Kit

THIS PAGE INTENTIONALLY LEFT BLANK

III. NICKEL RESULTS

This chapter discusses the results of the characterizing techniques on the sintered Nickel samples. Experiments were carried out to determine the optimal weight ratio of nickel powder and nickel oxide powder, properly activate the nickel powder, maximize the formation of self-sustaining support structures, and ensure that the final sintered nickel sample was fully reduced.

A. ACTIVATING THE NICKEL POWDER

There are different procedures and experiments available to activate metal powders. However, the most available method was the method described in the experimental methods. The nickel powder was placed in a 30% hydrogen peroxide bath and heated to 100 degrees Celsius for five minutes. In order to create the most self-supporting structures in the final low temperature casted sample, the nickel powder needed to be activated. Experiments conducted with non-activated nickel powder and nickel oxide produced weaker final products that did not hold their shapes and were not able to be handled. Confirmation of the activation of the nickel powder was difficult to obtain because the activation process described activates the nickel on the surface that is in contact with the hydrogen peroxide. The internal nickel powder remains un-activated. XRD analysis was performed on the powder after the activation process, shown in Figure 24.

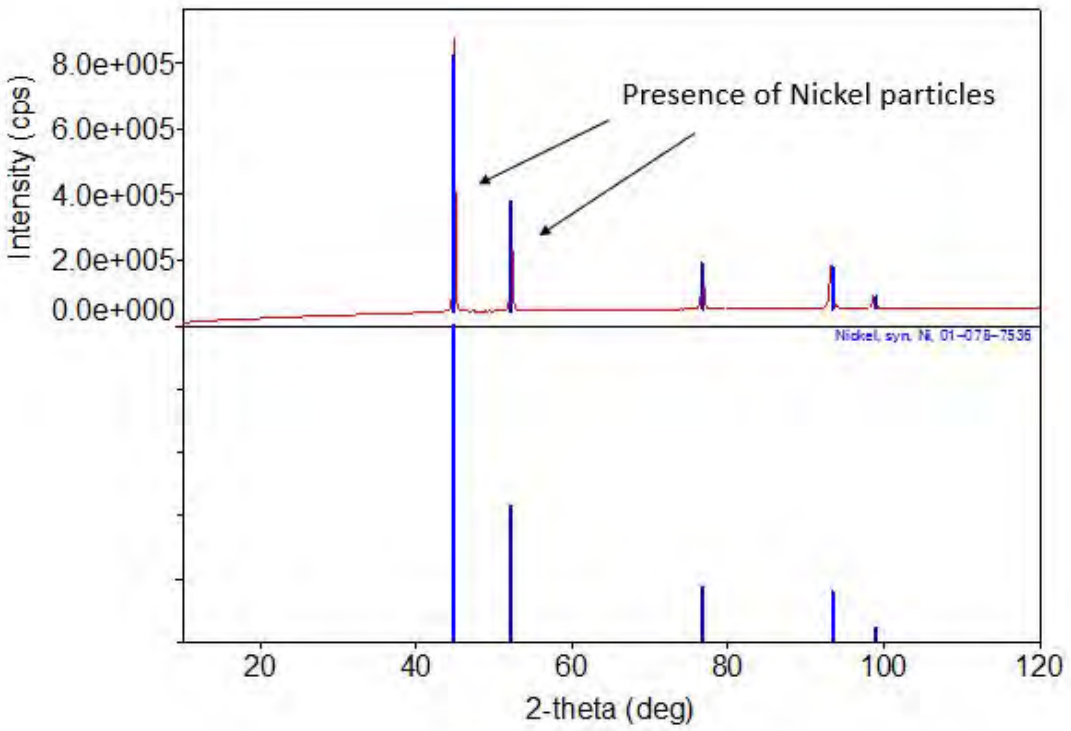

Figure 24. XRD Analysis of Ni After Activation Process

As depicted, the presence of modified Nickel was not shown in the XRD analysis of the metal; indicating that the activation process at most modifies a few layers of the particle surfaces. Yet, visual observation of evolving bubbles (Figure 25), shows a reaction is taking place. It is postulated that the peroxide reacts with carbon contamination on the particle surfaces, removing that material as oxide, and in the process generating hydrogen gas. Figure 26 shows the completed activation process approximately three minutes after removing nickel off the hot plate.

Figure 25. Activation Chemical Reaction

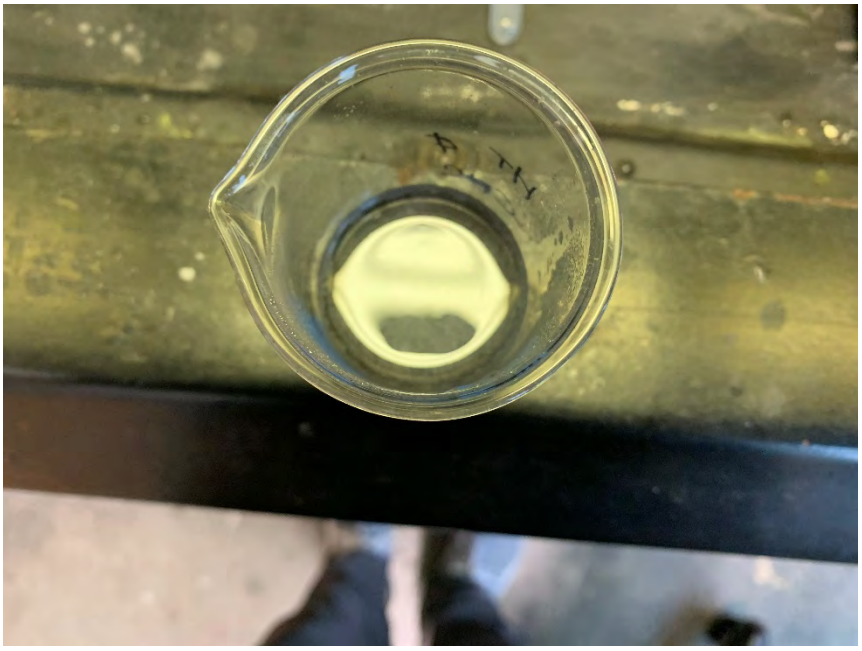

Figure 26. Completed Activation Process

B. METAL POWDER AND METAL OXIDE POWDER WEIGHT RATIO

The optimal weight ratio of nickel powder and nickel oxide powder was determined experimentally. The effectiveness of the trial was determined by the samples ability to hold shape and to be handled without falling apart. The nickel powder particle size for all of the experiments was 5 microns. Table 1 shows the different ratios that were tested and the results from the buoyancy tests.

Table 1. Weight Ratios Experimental Results for Nickel

Composition Ni:NiO:Urea, Percent NiO by weight	Oxygen Present after firing	~ Percent Metallic Ni by XRD inspection	Self-supporting Green Body after one firing	% Density normalized to bulk Ni metal/ Buoyancy method	% Density normalized to bulk Ni metal/ after HIP treatment	Trials Conducted
10:1:5, 10% NiO, 1 bake	Yes	90	Yes	98	N/A	3
10:1:5, 10% NiO, 2 bake	Yes	90	Yes	95	N/A	3
4:1:5, 25% NiO, 1 bake	No	100	Yes	92	N/A	3
4:1:5, 25% NiO, 2 bake	No	100	Yes	93	N/A	3
2:1:5, 50% NiO, 1 bake	No	100	Yes	96	94, 93	3

Self-supporting structures did not form on pure powders of Ni or NiO. Only mixture of nickel and nickel oxide powder developed self-supporting structures. The 50 percent by weight nickel oxide and nickel, the 2:1:5 ratio, sample appeared to form the strongest self-supporting structures based on a rather qualitative “snap” test (Figure 27 and 28).

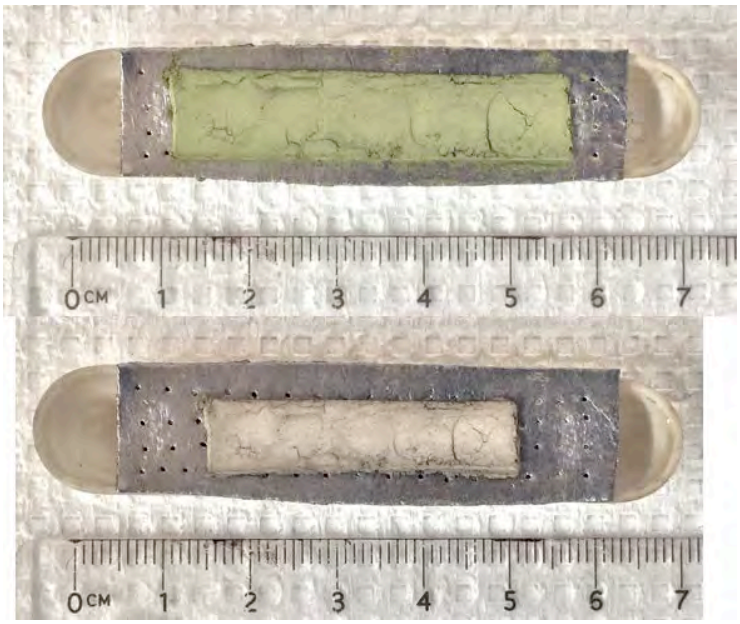

Figure 27. Before and After of 50% by Weight Nickel Oxide

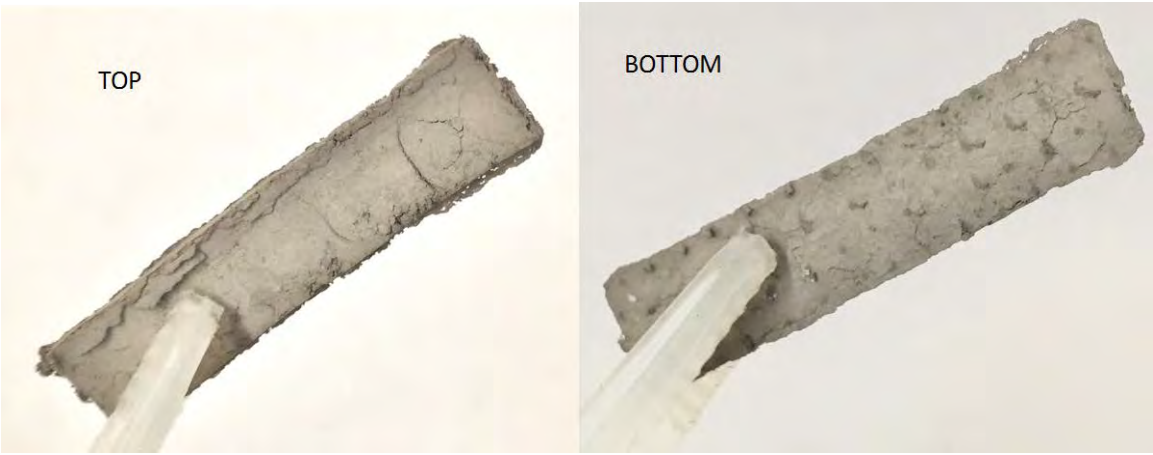

Figure 28. Self-Supporting Fully Reduced Nickel Bodies

C. FULL REDUCTION CONFIRMATION

The reduction of the activated nickel powder surface and the nickel oxide powder is fundamental in creating self-supporting structures. The self-supporting structures allow for the created samples to be able to be handled and retain their shape.

A simple mechanism is postulated to explain the need for metal and metal oxide particles. STEP 1: The thermal decomposition of urea produces radical species. STEP 2:

Radicals interact with the oxygen on the activated nickel powder or nickel oxide to form volatile oxides like carbon dioxide, leaving behind reduced metal atoms. STEP 3: The metal atoms migrate/diffuse until they encounter an existing crystal (metallic Ni), where they "snap" into place; enlarging the original metal crystal. This postulated step is essentially the same as that widely understood to be the mechanism by which crystals form from a supercooled liquid melt once nuclei are present. In the model employed in this work, the existing metal particle can be considered the "nuclei," and the metal atoms released during the reduction process at a temperature far below the melting temperature, a super-saturated solution.

The full reduction of the samples that was hypothesized to occur in the furnace was confirmed using XRD. The XRD results for the 25% NiO and 50% NiO are shown in Figure 29. Twice bake refers to the sample being put in the furnace with the same amount of urea to ensure full reduction.

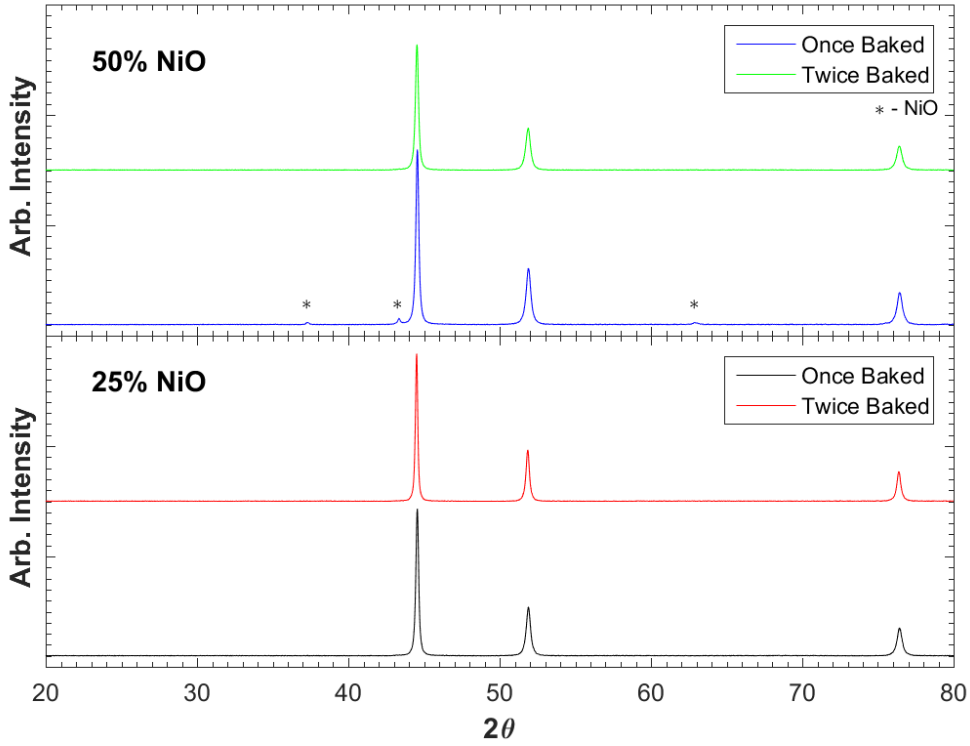

Figure 29. Nickel Sample XRD Analysis

The XRD analysis of the 25% NiO showed some signs of NiO remaining after the first bake, the XRD suggested ~90% reduction to metallic nickel. However, after the second bake the sample was completely reduced and there was no evidence of any remaining oxygen particles. The 50% NiO sample was fully reduced after the first bake and the XRD suggested ~100% reduction to metallic nickel. A second bake was conducted and examined; no change was found to the sample.

D. MORPHOLOGY INVESTIGATION

With the successful fabrication of a fully reduced sample that held its shape and was able to be handled, the next phase of validation of the RES-SM process involved investigating how the sample was being held together.

1. Self-supporting Structures between Nickel Particles

The self-supporting structures created by the RES-SM technique were observed using the SEM on the nickel sample. It can clearly be observed (Figure 30) that the final structure consists of particle connected by metal “necks” with void space between. Specifically, the RES-SM process creates necks that bind metal particles together. A virtually identical structure, metal particle joined by metal necks, is typically found in beds of metal particles heated sufficiently to sinter the metal particles together [25–28]. Similar to the present result, sintered masses of solid particles generally have more void space than solid metals created by nucleation and solidification from a liquid.

The RES-SM process created necks between the nickel particles. These necks provide evidence of sintering in the sample. The nickel particles are originally less than 5 microns in length before the RES-SM process. After the RES-SM process necks form between nickel particles that increase their total length. The nickel sample was investigated at different magnification, presented in Figure 30 and 31, to provide further insights on the morphology of the sample. Voids are still present in the sample; however, voids are expected after sintering together particles.

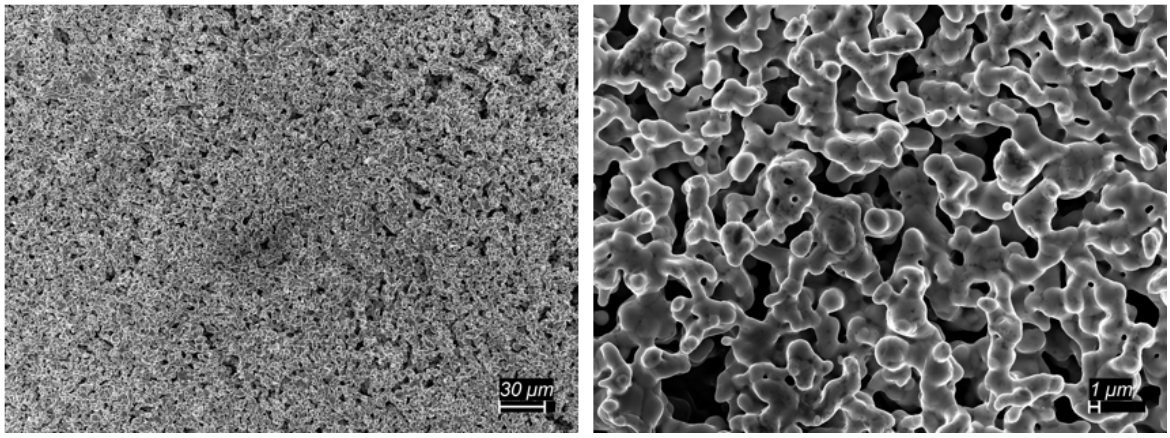

Figure 30. Nickel Sample after RES-SM Process 300x (left) 2,000 (right) Magnification

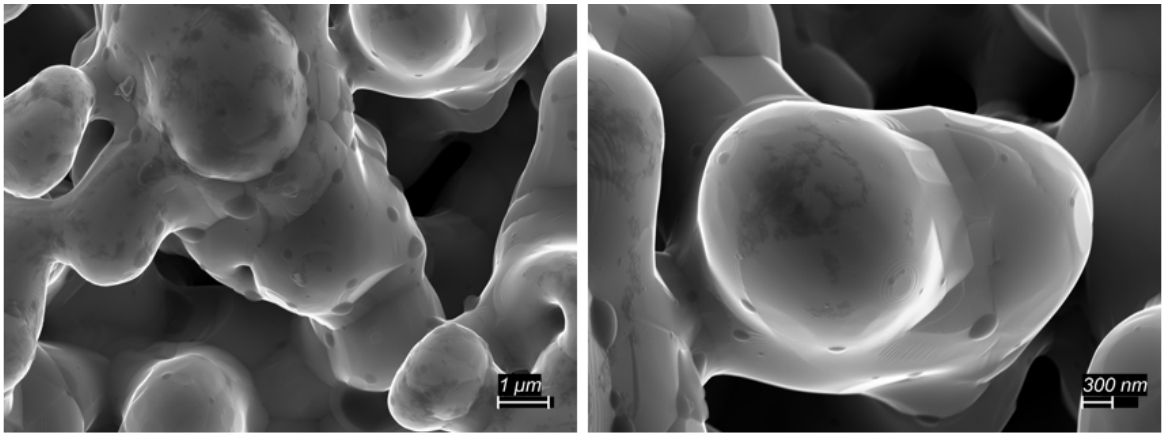

Figure 31. Nickel Sample after RES-SM Process 10,000x (left) 20,000x (right) Magnification

2. Void Density Investigation.

The nickel sample created after the RES-SM was polished in order to create a flat surface to be investigated with the optical microscope. Under the optical microscope the porosity of the sample could be evaluated. All the images taken in the optical microscope that were evaluated were taken at 20x magnification. ImageJ, an imaging processing software, was used measure the void density of the samples directly after the RES-SM process. ImageJ is able to accomplish this by converting the raw image pixels to binary bits that are black and white. The black binary bits represent the voids. ImageJ is then able

to compare the counts of black bits to white bits and calculate the porosity of the sample. The raw optical image and binary image are shown in Figure 32 for the nickel sample. The porosity of the nickel sample was calculated to be 4.5%.

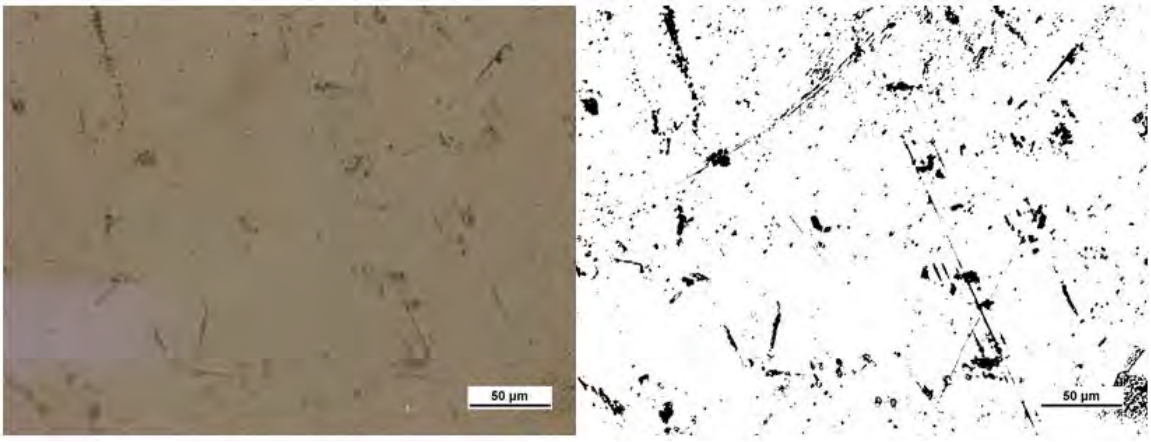

Figure 32. Nickel Raw Optical Image (left) and Binary Image (right) at 20x Magnification

The porosity calculated by ImageJ was higher than a sample made by casting, but lower than most green bodies. The distribution of pores also provides insight. In particular, the green body prior to HIP shows a nearly uniform distribution of small pores, and the pores are as large or smaller than the average metal particle, ca. 5 microns. After the HIP process polished samples indicate there are relatively large areas with no pores. This suggests ImageJ calculated relatively low porosities for the nickel sample possibly due to the polishing process of the sample making the surface a bad representation of the sample with regards to porosity.

In order to obtain a second density determination, nickel sample density was measured using the Ohaus Density Determination Kit. The analysis was done at 20.2 degrees Celsius, room temperature. The liquid used for the analysis was Ethanol with a density of $0.78917\frac{g}{cm^3}$. The density of air at this temperature was $0.0012\frac{g}{cm^3}$. Table 2 shows the results of the analysis. The results were compared to the accepted density values for nickel. From the accepted values the percent density was calculated.

Table 2. Density Measurement Results

Sample	Measured Density ($\frac{g}{cm^3}$)	Accepted Density Values ($\frac{g}{cm^3}$)	Percent Density (%)	ImageJ Percent Density (%)
Nickel 50% NiO	8.552	8.908	96	95.5

The measured densities are similar to those obtained from ImageJ evaluation of the light microscopy images. This suggests the "green parts" obtained from the RES-SM process are more dense than those created by standard binder techniques, in which the green density is generally less than 70% before full densification [29,30]. This outcome is not certain as there are clear sources of error from both techniques. Some possible errors in measuring density using the Ohaus density determination kit include the sensitivity of the scale. The scale only recorded to the fourth decimal place and all of the samples weighed less than one gram to obtain a more accurate measurement a more sensitive scale would have to be used. Sometimes bubbles form on the sample during the analysis which had to be brushed off. If these bubbles were not completely brushed off, then it would affect the density measurement. Figure 33 shows the sample being analyzed using the density kit.

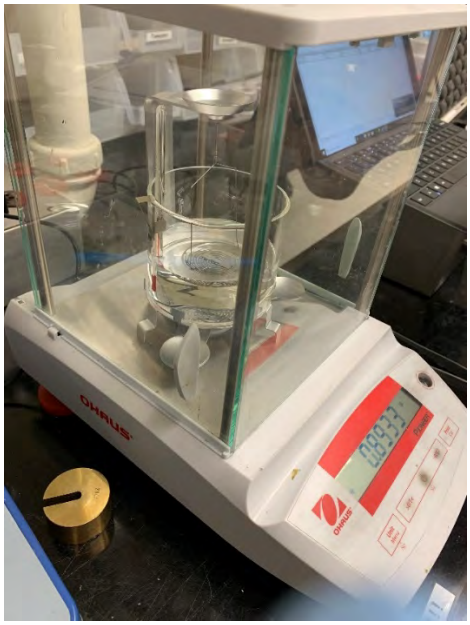

Figure 33. Nickel Sample in Ethanol Bath for Density Measurement

E. SHAPE CREATION

After successfully creating sintered fully reduced samples, the ability to create shapes using molds was investigated. Plastic molds were used to shape the powder into a tensile specimen with a shape/geometry similar than the one recommended by ASTM E8 shape. A tensile geometry was decided upon because it provided a somewhat complex shape and it is the ideal shape for stress testing. Figure 34 shows the mold used to produce the desired geometry. The plastic molds were printed on an Ultimaker 3 Extended 3D printer using a PLA filament with a 2.85 mm diameter.

Figure 34. Mold to Produce Tensile Test Geometry

The nickel sample was successfully molded into the tensile specimen geometry shape using the mold. The experiments involved packing the mixed powders into the mold and then carefully removing the mold. The pre-bake sample with the mold removed is presented in Figure 35. The nickel sample was sintered from nickel powder and fifty percent by weight nickel oxide powder. The nickel sample was able to hold its shape while maintaining clean and sharp edges. The shape does contain surface imperfections in the form of indents, however, the overall shape is true to the mold. Figure 36 shows the post RES-SM process nickel tensile test geometry sample. The nickel sample is fully reduced and the original shape retained, but clearly significant shrinkage occurred. Shrinkage is

present after the firing process in the RES-SM process. Several measurements were taken along the long and short axes, and these indicated that the shrinkage occurred evenly. That is, the relative value of all geometric factors, for example length/thickness, remained constant. In fact, every dimension of the tensile test geometry after the RES-SM process was 75+/-3% of the original particles-only body.

Figure 35. Pre-Bake Nickel Sample with the Mold Removed

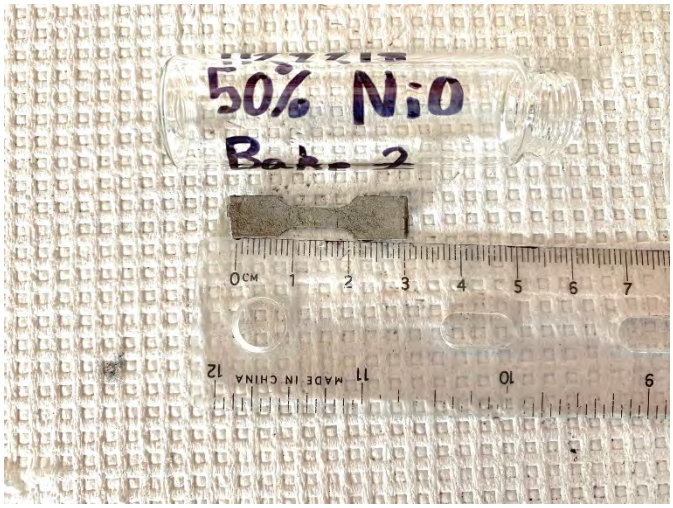

Figure 36. Nickel Tensile Test Geometry After RES-SM Process

After the RES-SM process the samples are considered green samples and require post process manufacturing to completely densify. These green samples do not have the same strength, electrical conductivity, thermal conductivity, ductility, and other physical properties of metal when contrasted to the nucleation and solidification from a liquid. In order to achieve the desired physical properties, the post RES-SM process nickel sample was sent to American Isostatic Presses (AIP) for hot isostatic pressing (HIP). The HIP process involves exposing the sample to elevated temperatures and pressures in a controlled gas atmosphere. The sample was placed in the heating chamber and the temperature was increased to 1000 degrees Celsius. The pressure was increased to 138 MPa The sample was left in the chamber at elevated temperature and pressure for 7 hours and then cooled. The purpose of the HIP testing is to fully densify the sample. The fully densified sample should have similar properties to a sample formed by nucleation and solidification from a liquid. The HIP treated sample was investigated using similar characterization methods.

Images of the morphology of the nickel sample after HIP treatment were taken using the SEM (Figure 37) and the images suggests HIP treatments changed the void structure fundamentally. Post HIP, on a local scale there are regions with virtually no voids. Clearly in places the particles fit together tightly, a morphology not observed prior to HIP. Figure 38 shows a comparison of the treated HIP sample and the sample directly after the RES-SM process at 10,000x magnification. The HIP treatment caused the particles to become closer together and produced stronger self-supporting structures.

In contrast the HIP samples also contain large voids (>10 micron) not observed prior to HIP. The observations of close fitting and void enlargement are consistent with void agglomeration. That is, the HIP process does not remove all the voids, but does favor the agglomeration of the voids.

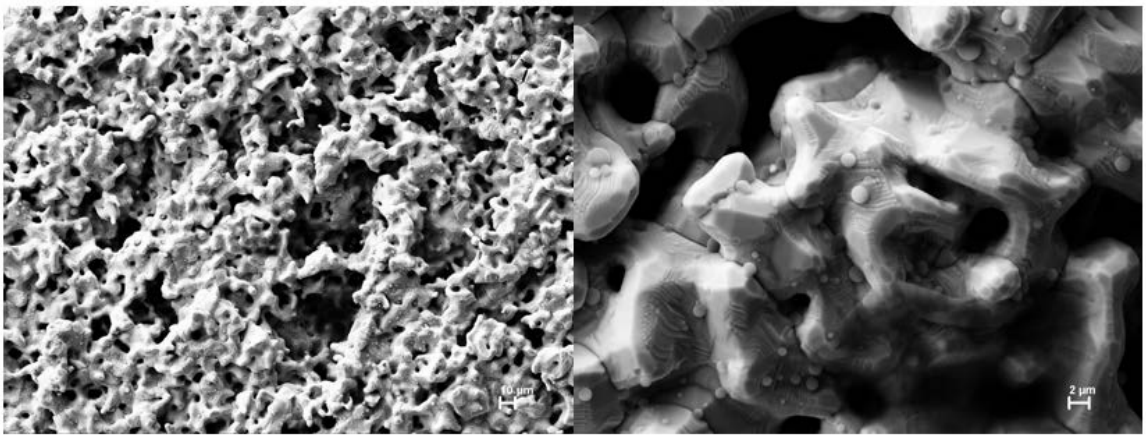

Figure 37. HIP Treated Nickel Sample 300x (left), and 2,000x (right) Magnification

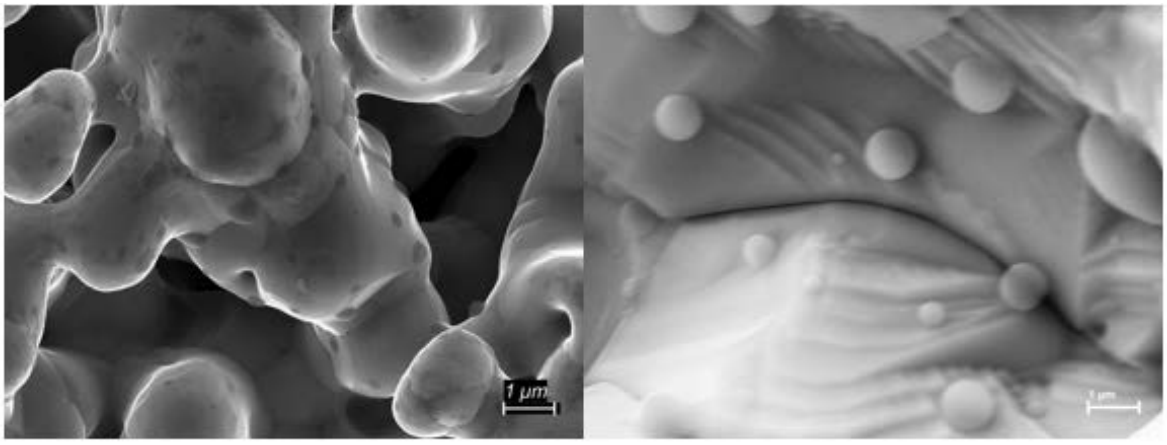

Figure 38. Non-HIP Treated Nickel Sample 10,000x (left), and HIP Treated Nickel Sample 10,000x (right) Magnification

This model was tested by investigating polished HIP treated nickel samples with the optical microscope. Under the optical microscope the porosity of the HIP treated samples could be evaluated. The images of the sample were taken at 20x magnification. Using ImageJ the void density of the HIP treated samples were calculated. Figure 39 shows the raw image and the black and white binary image of the HIP treated sample. The void density was measured to be ~8%. This result, and the buoyancy result (Table I) showing no net densification within experimental error due to HIP treatment, suggests there is no net decrease in void density due to HIP treatment. The result is consistent with the above suggestion that HIP treatment primarily leads to void agglomeration, not removal.

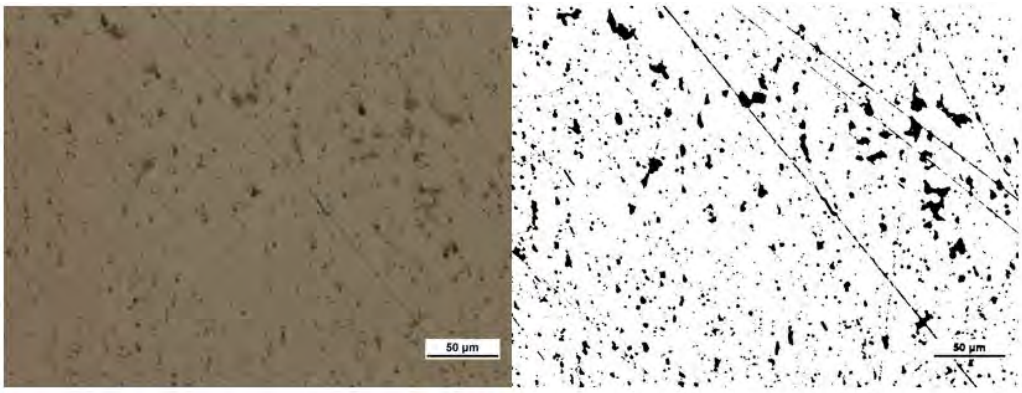

Figure 39. HIP Treated Nickel Raw Image (left), and Binary Image (right) at 20x Magnification

The results of a study of the polished HIP treated nickel sample using SEM are consistent with this model as well. The SEM images show regions with no voids, as well as some very large voids. There are also some very small (ca. 1 micron) pits and scratches attributable to the polishing process. The polished sample was also investigated using EDS, presented in Figure 41. The EDS analysis showed small traces of oxygen and carbon consistent with normal levels of surface contamination due to handling.

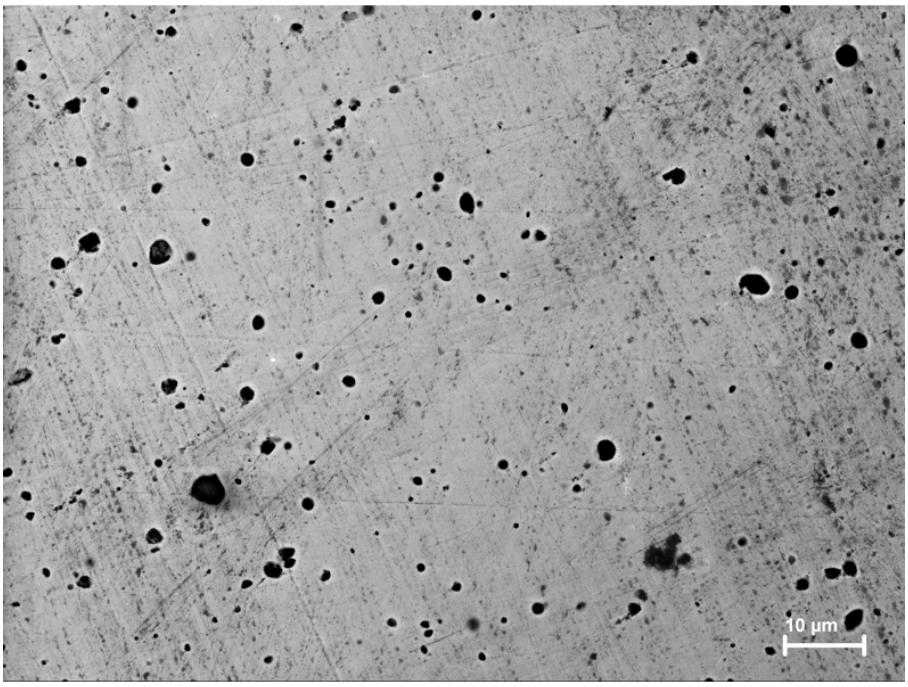

Figure 40. Polished HIP Treated Nickel Sample at 1,000x Magnification

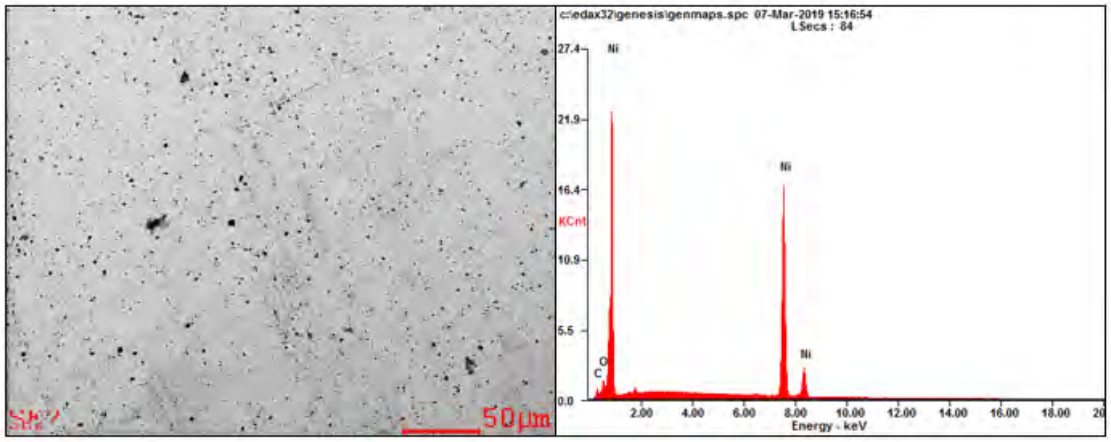

Element	Wt%	At%
CK	04.62	18.25
OK	02.19	06.48
NiK	93.19	75.27
Matrix	Correction	ZAF

Figure 41. Polished HIP Treated Nickel Sample EDS Analysis

The density of the HIP treated Nickel sample measured using the Ohaus density determination kit. The measurements were taken at room temperature (20.2 degrees Celsius). The liquid used in the analysis was Ethanol with a density of 0.78917$\frac{g}{cm^3}$. The density of air at this temperature was 0.0012$\frac{g}{cm^3}$. The results are contained in Table 3. The experimentally measured density of the HIP treated Nickel sample was compared with the accepted density value of pure nickel. Based on the accepted density value of pure nickel the percent density was calculated. The measured density of the HIP treated nickel sample was less than the measured density of the sample after the RES-SM process. This can be attributed to experimental error in the precision of the Ohaus density determination kit.

Table 3. Density Measurement Results for HIP Treated Nickel

Sample	Measured Density ($\frac{g}{cm^3}$)	Accepted Density Values ($\frac{g}{cm^3}$)	Percent Density (%)
HIP Treated Nickel	8.388	8.908	94.2

The tensile strength of the HIP treated nickel sample was taken using the Instron 4507 Tensile Tester in Figure 42. Using the Instron 4507 Tensile Tester involves mounting the sample in the clamps of the machine. The instrument then applies a tensile force in order to pull apart the sample. The instrument increases the force until the failure of the specimen. The deformation related to the applied force before failure is measured by the instrument. Knowing the area and length of the specimen before testing, the stress and strain can be calculated. Figure 43 shows the experimentally measured stress-strain curve. The stress and strain plotted in Figure 53 are the engineering stress and engineering strain because the change of area during deformation is not accounted for. The HIP treated nickel sample did not behave exactly as a nickel sample is expected to behave in a tensile test. However, the yield strength was experimentally measured to be 27.73 MPa. The yield strength of nickel varies depending on the processing treatments used. The generally accepted value for the yield strength is 59.0 MPa [31]. The difference is attributed to the nickel test specimen being too small for the tensile strength machine, resulting in the experimentally measured yield strength being inaccurate.

Figure 42. Instron 4507 Tensile Tester

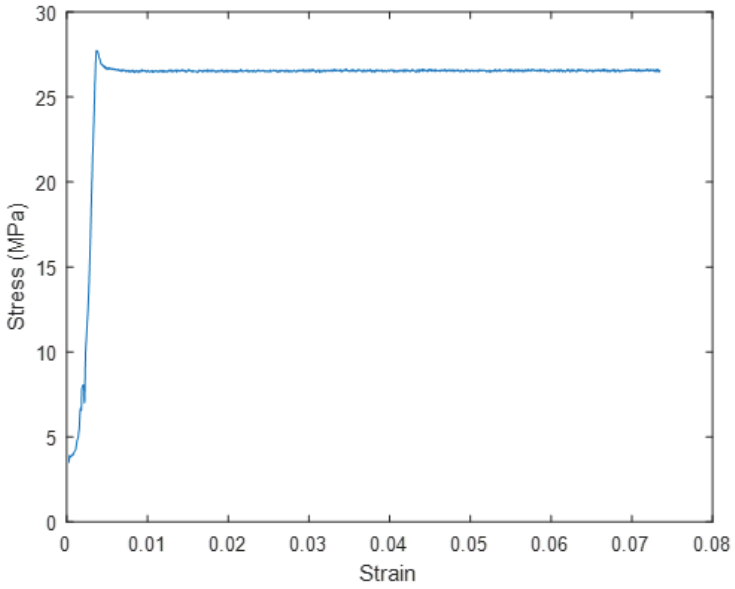

Figure 43. Stress-Strain Graph for HIP Treated Nickel Sample

A hardness test was conducted on the HIP treated nickel sample using the Struers DuraScan, presented in Figure 44. Five measurements were executed on different parts of the sample. The five measurements were averaged and the hardness of the sample was concluded to have a hardness of 86 on the Vickers hardness scale. Generally, the accepted Vickers hardness for pure cast but unworked nickel is between 81 and 90 [32–34]. The HIP treated nickel sample had acceptable hardness values as pure cast nickel, suggesting that the HIP treated nickel sample would have comparative mechanical properties as pure cast nickel.

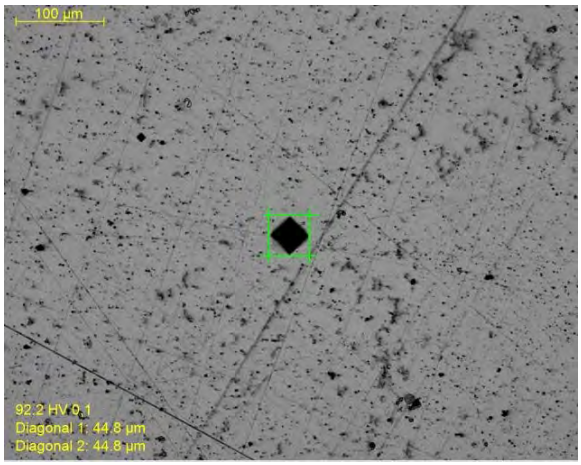

Figure 44. Hardness Test taken on Stuers DuraScan

IV. IRON RESULTS

This chapter discusses the results of the characterizing techniques on the sintered iron sample. Experiments were carried out to determine the optimal weight ratio of iron powder and iron oxide powder, properly activate the iron powder, maximize the formation of self-sustaining support structures, and ensure that the final sintered iron sample was fully reduced.

A. ACTIVATING THE IRON POWDER

The same approach described in the experimental methods was conducted to activate the iron powder. The iron powder was placed in a 30% hydrogen peroxide bath and heated to 100 degrees Celsius for five minutes. It was experimentally demonstrated that stronger self-supporting structures formed when the metal powder component of the compact was activated in the RES-SM process. It is postulated that the activation cleans the surface of hydrocarbon impurities, a supposition consistent with XRD (Figure 44) and EDAX studies that show no changes between the activated and unactivated sample. Clearly, only surface chemistry is modified. Also, the formation of large bubbles is consistent with CO, CO_2, etc., formation due to reaction between carbon contamination and the peroxide.

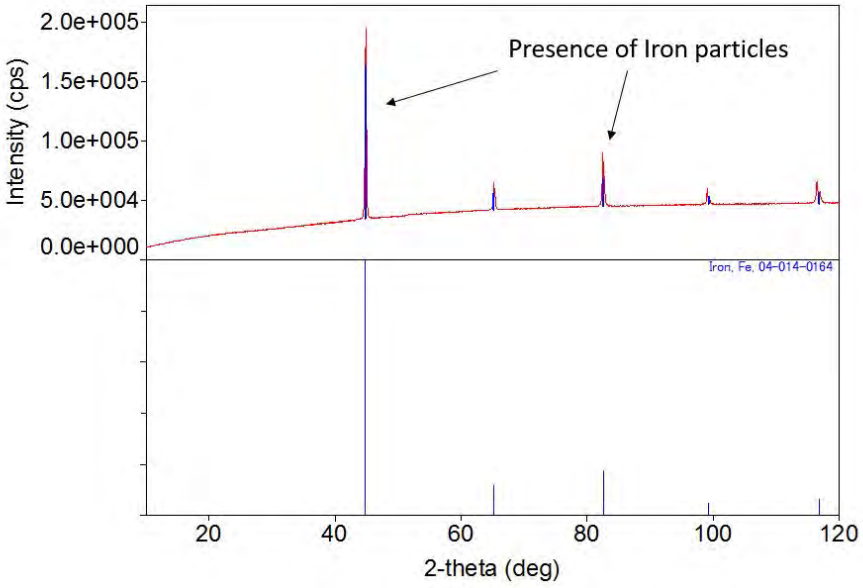

Figure 45. XRD Analysis of Iron After Activation Process

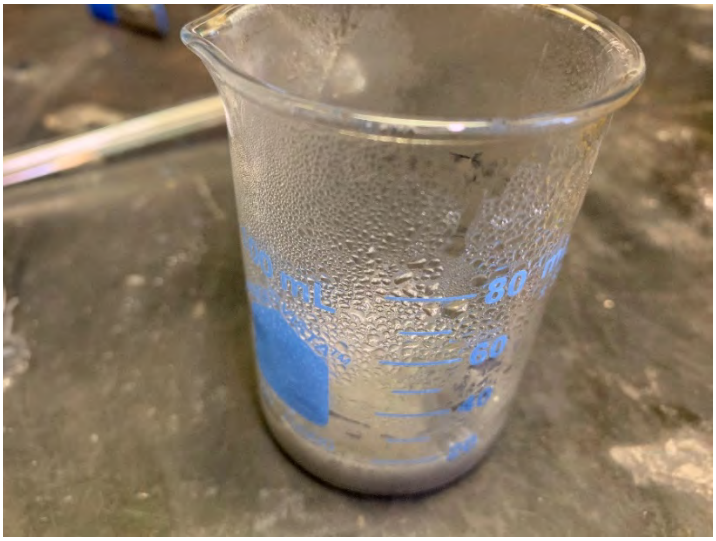

Figure 46. Completion of Activation Process

B. IRON POWDER AND IRON OXIDE POWDER WEIGHT RATIO

The optimal weight ratio of iron powder and iron oxide powder was determined experimentally. The effectiveness of the trial was determined by the sample's ability to hold its shape and its ability to be handled without falling apart. Different particle sizes were tested until the optimal particle size was determined. The experimental tests and

results are depicted in Table 4 for iron. The iron oxide powder used in all of the experimental trials had a particle size less than 6 nanometers in diameter.

Table 4. Weight Ratios Experimental Results for Iron

Weight Percentage FeO	Fe Particle Size	Description	Result
50%	>20 µm	Uniform grey, shape did not hold, formed into chunks, limited bonding	
40%	>20 µm	Uniform grey, shape did not hold, formed into chunks, limited bonding	
30%	>20 µm	Uniform grey, shape held better, sample crumbled when handled, some bonding	
25%	>20 µm	Uniform grey, shape held, able to be handled, evidence of bonding	
20%	>20 µm	Uniform grey, shape held, able to be handled, evidence of bonding	
15%	>20 µm	Uniform grey, shape held, evidence of some bonding	

Weight Percentage FeO	Fe Particle Size	Description	Result
10%	>20 µm	Uniform grey, sample held its shape, able to be handled, evidence of bonding	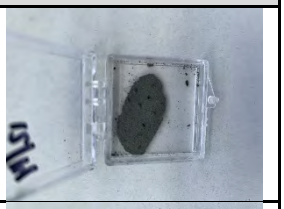
5%	>20 µm	Uniform grey, shape held, able to be lightly handled, evidence of bonding	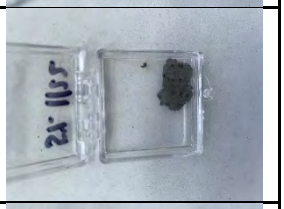
0%	>20 µm	Uniform grey, shape somewhat held, able to be lightly handled, evidence of bonding	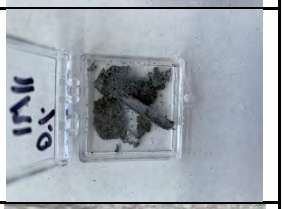
10%	<5 µm	Uniform grey, shape held, able to be handled, stronger evidence of bonding	
50%	<5 µm	Sample did not hold its shape, chunks formed, little evidence of bonding	

It was determined experimentally that the optimal weight ratio for the iron samples was the iron powder mixed with 10% by weight Iron Oxide powder. When the particle size of the iron powder was lowered to a finer grade, the resultant sample was qualitatively stronger and there was more evidence of self-supporting structures. The Sigma-Aldrich 5 micron powder produced the best results. Figure 46 shows a comparison of the 10% FeO iron sample and the 50% FeO iron sample. The 10% FeO iron sample held its shape and preformed best in the qualitative “snap” tests. The 50% FeO iron sample was unable to hold its shape, however there is evidence of some self-supporting structures between the iron particles.

Figure 47. 10% FeO Iron Sample (left) and 50% FeO Iron Sample (right)

C. FULL REDUCTION CONFIRMATION

Reducing the iron sample to ~100 percent metallic iron was necessary to create the strongest samples with the most self-supporting structures. The increase in self-supporting structures allows the sample to retain its shape and to be handled. It was hypothesized that the thermal decomposition of urea produced radical species that were capable of reducing the iron oxide particles. The mechanism is assumed to be virtually identical to that discussed in detail in the preceding chapter. XRD was used to confirm the full reduction of the 10% by weight FeO iron sample, presented in Figure 47. The XRD analysis showed no evidence of any oxygen particles in the iron sample.

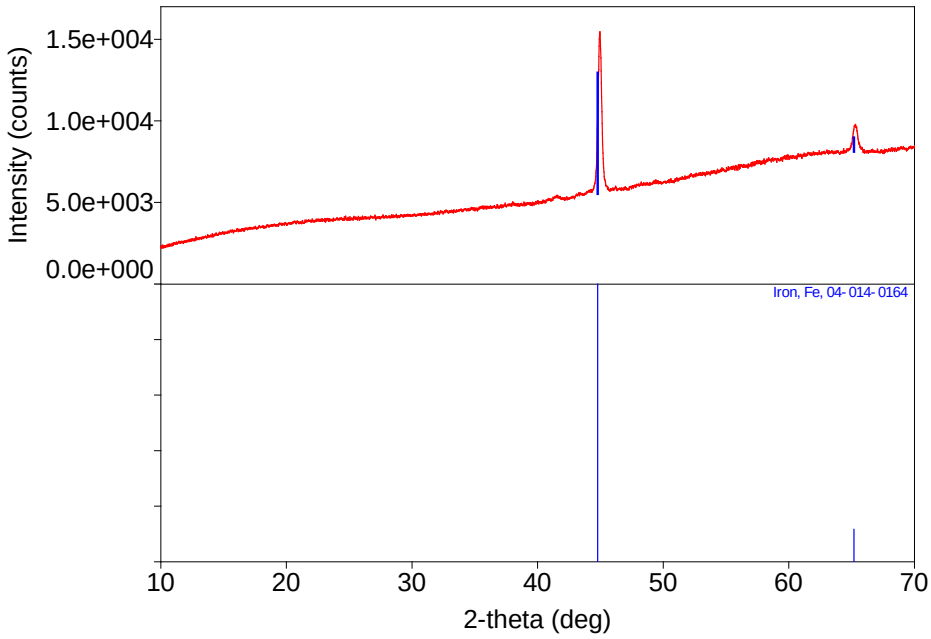

Figure 48. Iron Sample XRD Analysis

D. MORPHOLOGY INVESTIGATION

1. Self-supporting Structures between Iron Particles

The self-supporting structures created by the RES-SM technique were observed using the SEM on the 10% FeO by weight iron sample. Again, as in the Ni/NiO case, the RES-SM process creates structures consisting of original iron particles connected by "necks," with clear evidence of large pores, that is void spaces. These void spaces appear larger than those found in solids formed by nucleation and solidification from a liquid melt; however, the overall structure is similar to that observed when metal particles are thermally sintered.

The Sigma-Aldrich 5 μm, 99.5% purity iron powder was taken from the bottle, mounted to a viewing mount and observed in the SEM to provide a comparison to the finished sintered masses after the RES-SM process. The iron powder consists of particle sizes less than five microns. Before the RES-SM process the particles have no association with each other and there are no signs of necking or bonding between the particles. The iron powder before the RES-SM process shows significant space in between the particles

and the particles are round spherical shapes. The difference in brightness of the particles in Figure 48 signifies iron particles at different depths in the powder. The image on the left was taken at 2,000x magnification and the image on the left was taken at 8,000x magnification.

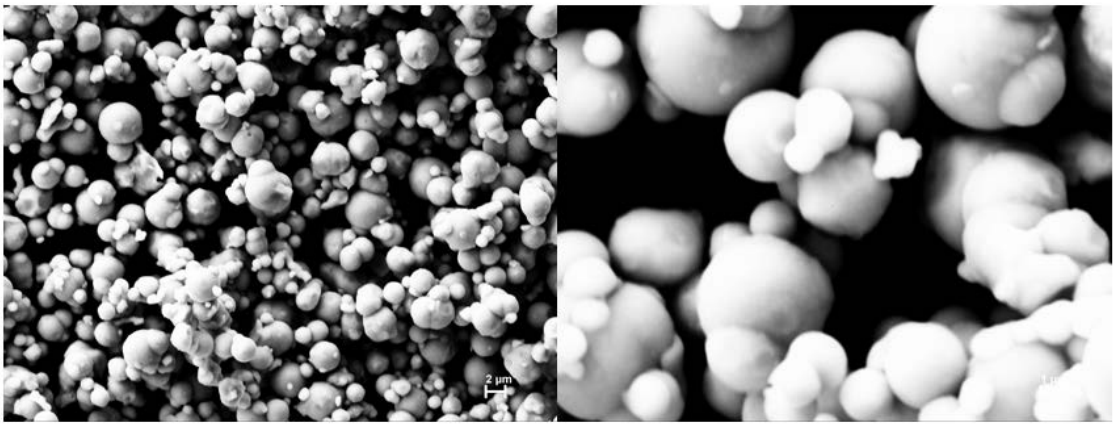

Figure 49. Micron Sized Iron Powder Out of the Bottle before the RES-SM Process

Figure 49 and 50 show the SEM images of the iron sample after the RES-SM process. It is apparent that the RES-SM process does cause bonding in the form of necking between the iron particles. When the iron particles sinter together after the RES-SM process the particles loose part of their spherical shape and necks form between them. The iron sample is fully reduced after the RES-SM process and it is pure iron that is bonding together. Most of the iron particles are generally bonded with two or more of the surrounding particles. There are still voids, the black spaces in Figure 49 and 50, in the sample after the RES-SM process. The SEM analysis of the experimental sample proved that the RES-SM process caused sintering to occur between the metal particles. Void space is a common result of sintering particles together.

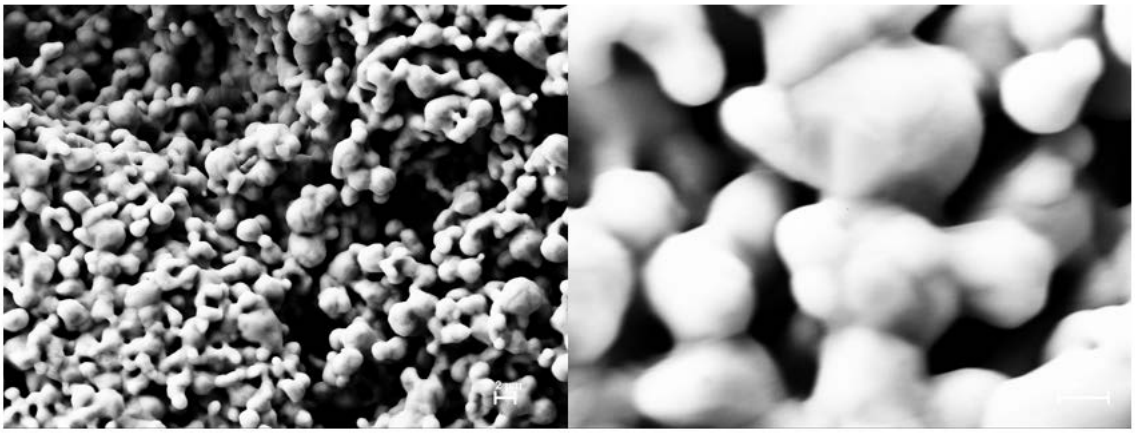

Figure 50. Iron Sample after RES-SM Process 2,000x Magnification (Left), 10,000x Magnification (Right)

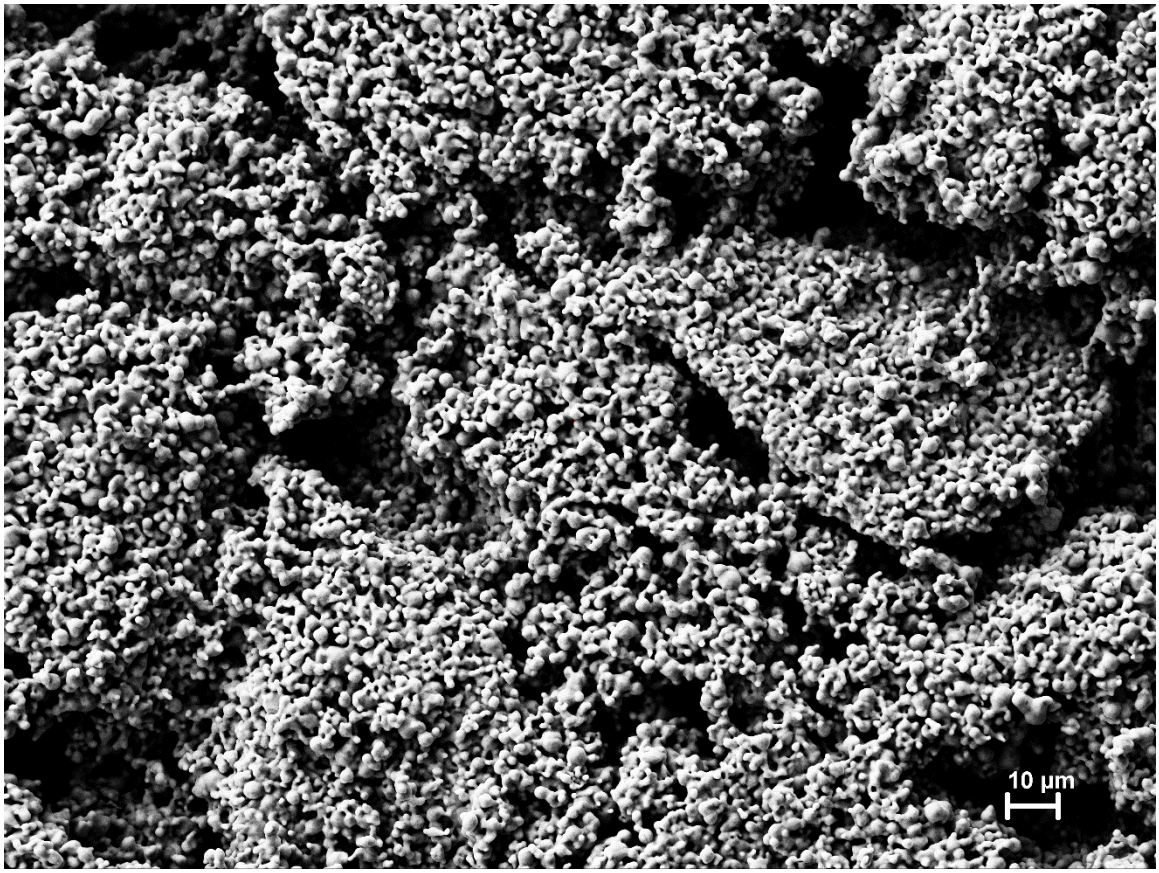

Figure 51. Iron Sample after RES-SM Process 500x Magnification

2. Void Density Investigation

The 10% FeO by weight iron sample was polished in order to investigate the porosity of the sample with an optical microscope. The images taken with the optical microscope to measure porosity were taken at 20x magnification. Similarly to the nickel sample, the porosity was measured using ImageJ. Figure 51 shows the raw optical image of the iron sample and the binary image of the iron sample. ImageJ measured the porosity of the iron sample to be ~7%. The iron sample is a "green body," but there are not large pores. Contrasted with the HIP treated nickel sample the iron sample had a smaller porosity.

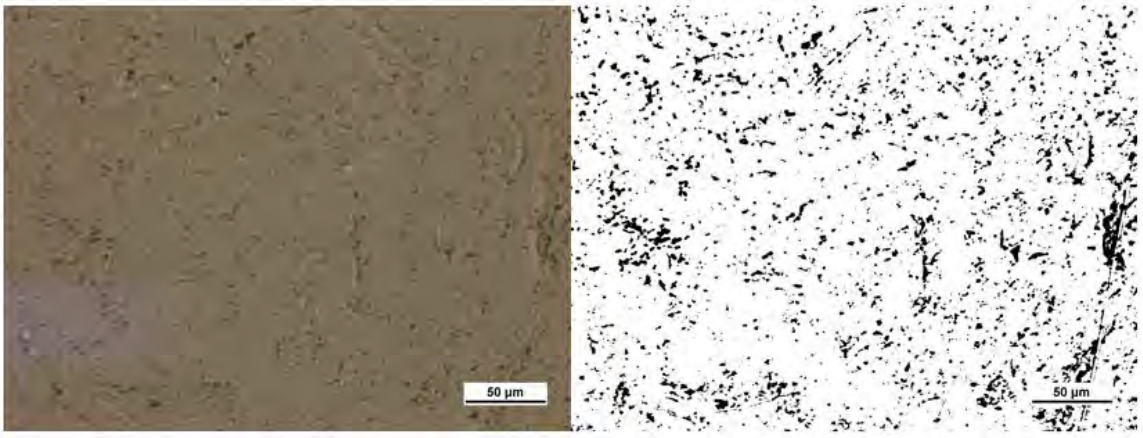

Figure 52. Iron Raw Optical Image (left) and Binary Image (right) at 20x Magnification

The density of the 10% FeO sample was measured using the Ohaus density determination kit. The analysis was done at 20.2 degrees Celsius, room temperature. The liquid used for the analysis was Ethanol with a density of $0.78917\frac{g}{cm^3}$. The density of air at this temperature was $0.0012\frac{g}{cm^3}$. Table 5 shows the results of the density analysis using the Ohaus density determination kit along with the results from the ImageJ investigation. The measured density was higher than anticipated, especially because the samples after the RES-SM process are considered green parts and are not fully densified. The possible errors of the Ohaus density determination kit have already been discussed.

Table 5. Density Measurement Results for Iron Sample

Sample	Measured Density ($\frac{g}{cm^3}$)	Accepted Density Values ($\frac{g}{cm^3}$)	Percent Density (%)	ImageJ Percent Density (%)
Iron 10% FeO by weight	7.785	7.874	98	93

E. SHAPE CREATION

Numerous experiments were ran trying to create the tensile test geometry shape using iron powder and ten percent by weight iron oxide powder. The experiments involved packing the mixed powders into the mold and then carefully removing the mold. Figure 52 shows the RES-SM process sample and Figure 53 shows the post RES-SM process. As presented in Figure 53 the sample was able to somewhat hold the shape, however the edges are not sharp and it is not a precise sample. The iron samples were not able to hold a clean and precise shape using the mold method. The samples were fully reduced and there was evidence of self-supporting structures. The casting process needs to be refined in order to successfully cast iron into precise shapes using the RES-SM process.

Figure 53. Iron Tensile Test Geometry Shape Before RES-SM Process

Figure 54. Iron Tensile Test Geometry Shape Before RES-SM Process

THIS PAGE INTENTIONALLY LEFT BLANK

V. CONCLUSION

This final section explores the results and goals that were accomplished in this research. It provides insights in the fabrication process and the conclusions from the materials characterization processes. This section includes recommendations for future works.

A. ACHIEVEMENTS

A new and novel method of creating sintered metal bodies far below the melting temperature was discovered and explored. The RES-SM process proved to be able to produce fairly high density green bodies that are fully metal. Initial post processing studies with the HIP process show little density increase, but do show the removal of small pores, and the agglomeration of large pores.

The researched concluded that the powder could be shaped before being placed in the furnace. The shapes could be cast using 3D printed plastic “molds.” The powder held its shape during the RES-SM process and was able to be maneuvered and handled. The sample after the RES-SM process was not fully densified and did not have the same physical characteristics as pure metal with respect to tensile strength. The nickel samples were able to produce clean and sharp shapes. The iron samples were not able to produce clean shapes which is attributed to the casting process.

The optimal weight ratios of metal powder and metal oxide powder were determined experimentally. The optimal weight ratio for the iron samples was ten percent iron oxide. The optimal weight ratio for the nickel samples was fifty percent nickel oxide. The experiments were carried out using 0.5 grams of urea.

The RES-SM process produced sintered particles at a temperature of 900 degrees Celsius which is hundreds of degrees below the melting temperature of iron and nickel. The particles were held together by self-supporting structures in the form of necks between the particles. There was still evidence of voids between the particles and the sample was not fully densified.

It was determined experimentally that the size of the metal powders affected the outcome of the RES-SM process. More successful trials were accomplished using a finer metal powder, typically a powder with a particle size less than six microns. The particle size in the powder affected the oxidation process and how many self-supporting structures formed in the RES-SM process.

B. FUTURE WORK

While there were significant research questions answered in this study, there remains the possibility for future advancements and refinements to the RES-SM process and the shape casting process.

The activation of the metal powder process could be adjusted. The metal powder was activated using 30% hydrogen peroxide and heat. This method only activates the metal elements on the outside of the metal particles and it does not activate the internal elements in the metal particles. Identifying or discovering a new process to activating metal powder that yields a higher activation percentage could improve the amount of self-supporting structures and reduce the porosity of the samples.

The furnace and quartz tube used in this research had a limit of 0.5 grams of urea because samples with more than 0.5 grams of urea caused a pressure build up and the sample would cause the fasteners on the pipe to loosen and expose samples to air. Using a different furnace that allows for a larger quartz tube could allow for more urea to be used which could cause more self-supporting structures to develop.

For the iron samples a sharp complex shape was unachievable. The shortcomings of the iron samples were attributed to the casting process. The casting process could be investigated and perhaps using some type of adhesive material or lubricant on the 3D printed plastic part the iron powder could be shaped more successfully.

LIST OF REFERENCES

[1] Bandyopadhyay, Amit., and Bose, Susmita. Additive Manufacturing. Taylor and Francis, Hoboken, NJ (2015).

[2] 3D Printing Media Network “The global additive manufacturing market 2018 is worth $9.3 billion” Accessed April 24, 2019 [Online]. Available: https://www.3dprintingmedia.network/the-global-additive-manufacturing-market-2018-is-worth-9-3-billion/

[3] Srivatsan, T. S., and Sudarshan, T. S. Additive Manufacturing. 1st ed. CRC Press, Boca Raton, FL (2015).

[4] 3D HUBS “Introduction to Metal 3D printing” Accessed April 24, 2019 [Online]. Available: https://www.3dhubs.com/knowledge-base/introduction-metal-3d-printing

[5] U.S. Food & Drug Administration “Medical Applications of 3D Printing” Accessed April 24, 2019 [Online]. Available: https://www.fda.gov/medicaldevices/productsandmedicalprocedures/3dprintingofmedicaldevices/ucm500539.htm

[6] 3DEO, “Understanding Surface Finish in Metal 3D Printing” Accessed May 2, 2019 [Online]. Available: https://news.3deo.co/metal-3d-printing-surface-finish

[7] 3D Printing, “Ultimaker 3 Extended” Accessed May 2, 2019 [Online]. Available: https://3dprinting.com/pricewatch/3d-printer/ultimaker-3-extended/

[8] Sciaky Inc. “Electron Beam Additive Manufacturing (EBAM)” Accessed April 25, 2019 [Online]. Available: http://www.sciaky.com/additive-manufacturing/metal-additive-manufacturing-systems

[9] ANIWAA “EBAM 300 Series Sciaky” Accessed May 2, 2019 [Online]. Available: https://www.aniwaa.com/product/3d-printers/sciaky-ebam-300-series/

[10] Davis, J. R. “Fusible Alloys.” 2nd edition. ASM International, Materials Park, OH (1998). 1–1. Print.

[11] America’s Navy Forged By The Sea “Seabees Deploy With Additive Manufacturing Capabilities” Accessed April 25, 2019 [Online]. Available: https://www.navy.mil/submit/display.asp?story_id=108627

[12] The Maritime Executive “U.S. Navy Installs First 3D-Printed Metal Part Aboard a Warship” Accessed April 25, 2019 [Online]. Available: https://www.maritime-executive.com/article/u-s-navy-installs-first-3d-printed-metal-part-aboard-a-warship

[13] 3DPrint.com “The USS Harry S. Truman: Metal 3D Printing to Play a Role in Designing Navy Warships” Accessed April 25, 2019 [Online]. Available: https://3dprint.com/235066/uss-harry-s-truman-metal-3d-printing-to-play-a-role-designing-navy-warships/

[14] Zea, H, Luhrs, Cc, and Phillips, J. “Reductive/expansion Synthesis of Zero Valent Submicron and Nanometal Particles.” Journal Of Materials Research 26.5 (2011): 672–681. Web.

[15] C. C. Luhrs, J. Phillips, “Reductive-expansion synthesis of graphene,” U.S. Patent 8 894 886, Mar. 4, 2011

[16] Canty, Russell et al. Reduction Expansion Synthesis as Strategy to Control Nitrogen Doping Level and Surface Area in Graphene. N.p., 1621. Print.

[17] Luhrs, Claudia et al. “Novel Process for Solid State Reduction of Metal Oxides and Hydroxides.” Metallurgical and Materials Transactions B 44.1 (2013): 115–122. Web.

[18] Pelar, Christopher J. Reduction Expansion Synthesis of Chromium and Nickel Metal Coatings. Monterey, California: Naval Postgraduate School. Print.

[19] Lee, Tongli Lim et al. High-Stability Tin/carbon Battery Electrodes Produced Using Reduction Expansion Synthesis. Elsevier Ltd., 2018. Print.

[20] He, Bob B. Two-Dimensional X-Ray Diffraction. Hoboken, NJ: Wiley, 2009. Print.

[21] Seeck, Oliver H., and Murphy, Bridget M. X-Ray Diffraction : Modern Experimental Techniques . Boca Raton, Florida: Pan Stanford Publishing, 2014. Print.

[22] Ross Richard J. “Optical Microscopy.” Microelectronics Failure Analysis Desk Reference. 6th Edition. ASM International, 2011. 1–1. Web.

[23] Leng, Yang. “Scanning Electron Microscopy.” Materials Characterization. Weinheim, Germany: Wiley-VCH Verlag GmbH & Co. KGaA, 2013. 127–161. Web.

[24] SURF, “Scanning Electron Microscopy and Energy Dispersive X-Ray Spectroscopy” Accessed April 12, 2019 [Online]. Available: www.surfgroup.be/semedx.

[25] J. Phillips, ‘Chemical Method To Create Metal Films On Metal And Ceramic Substrates’ Non-provisional patent 20160012 (2017).

[26] German, R.M. (1994) Powder metallurgy science, in Metal Powder Industries Federation, 2nd edn, Princeton, New York.

[27] Suk-Joong L. Kang (2004) Sintering: Densification, Grain Growth, and Microstructure, 1st edn, Butterworth-Heinemann (available via ScienceDirect)

[28] Coble, R. L., A model for boundary diffusion controlled creep in polycrystalline materials, J. Appl. Phys., 34, 1679–82, 1963.

[29] Engineering, “HP Announces Metal Jet 3D Printing at IMTS” Accessed May 24, 2019 [Online]. Available: https://www.engineering.com/3DPrinting/3DPrintingArticles/ArticleID/17617/HP-Announces-Metal-Jet-3D-Printing-at-IMTS.aspx

[30] Engatech R&D, “A Look at Metal 3D Printing” Accessed May 14, 2019 [Online]. Available: http://engatech.com/metal-3d-printing/

[31] MatWeb Material Property Data, “Nickel, Ni” Accessed April 22, 2019 [Online]. Available: www.matweb.com/search/DataSheet.aspx?MatGUID=e6eb83327e534850a062dbca3bc758dc&ckck=1

[32] AZoM, “Properties: Nickel - Properties, Fabrication and Applications of Commercially Pure Nickel,” Accessed May 22, 2019 [Online]. Available: https://www.azom.com/properties.aspx?ArticleID=2193.

[33] F. Djavanroodi, M. Ebrahimi, and J. F. Nayfeh, “Tribological and mechanical investigation of multi-directional forged nickel,” Scientific Reports, vol. 9, no. 1, 2019.

[34] Element Nickel, Ni, Transition Metal, “Hardness of Nickel,” Accessed May 22, 2019 [Online]. Available: http://nickel.atomistry.com/hardness_of_nickel.html.

THIS PAGE INTENTIONALLY LEFT BLANK

INITIAL DISTRIBUTION LIST

1. Defense Technical Information Center
   Ft. Belvoir, Virginia

2. Dudley Knox Library
   Naval Postgraduate School
   Monterey, California